Chapter 5

Functionalized 2D-MoS_2 Nanosheets for Electrocatalytic Hydrogen Evolution Reaction via Water Electrolysis

5.1 Introduction

This chapter presents the development of sulfonic acid (-SO_3H) group functionalized 2D-MoS_2 nanosheets and their structural characterizations such as (Raman, FTIR, XPS, FESEM, TEM/HRTEM, TGA, DSC) followed by application for hydrogen evolution reaction (HER). Over the past few years, many potential alternatives for noble-metal-free electrocatalysts for hydrogen evaluation reaction (HER) have been exploited, including chalcogenides of cobalt [1], molybdenum [2, 3], tungsten [4], nickel [5], and a series of molecular catalysts [6]. Among these materials, molybdenum disulfide (MoS_2) has received tremendous attention due to its suitable Gibbs free-energy for hydrogen adsorption, earth-abundant, high electrocatalytic activity, low cost, and also has long-term stability in strongly acidic and alkaline conditions [7, 8]. Two-dimensional (2D) layered transition metal dichalcogenides (MX_2) are typically consist of M as a transition metal (Mo, W, V) and X as a chalcogen (S, Se, Te), where each MX_2 type layer (S-Mo-S layers) are stacked to each other and connected with the week van der Waals interaction [9-11]. Owing to the anisotropic structure, MoS_2 is likely to form two-dimensional (2D) morphology that offers a large surface area and 2D permeable channels for ion adsorption and transport [12-14]. Although in abundant form, however, 2D-MoS_2 lacks in intrinsic electrical conductivity owing to its bandgap (1.81 eV for monolayer and 1.27 eV for bulk), low carrier concentration, limited interlayer charge-transport, and restricted electron transfer at the interfaces.[15] Hydrogen evolution reaction (HER) activity of MoS_2 is localized to the rare edge surfaces, whereas the (0001) basal planes are relatively inactive, which significantly limits the overall HER performance. [16, 17]

Motivated by this understanding, intense research efforts have been focused on developing various 2D nanostructured MoS_2 based HER catalysts to maximize the number of exposed edge sites, including metallic 1T polymorph [18, 19], amorphous [20], and crystalline materials [21], vertically aligned structures [22, 23], and molecular mimics [24]. Besides

active sites, the intrinsic conductivity of catalysts is another crucial factor affecting the electrocatalytic activity because high conductivity ensures faster electron transport from the conductive substrate to active sites. Several efforts have been made to enhance the conductivity of MoS_2 include hybridizing with conductive substrates, especially carbonaceous materials such as rGO [25, 26], carbon nanotube [27, 28], carbon fiber [29], carbon cloth [30], and hollow carbon sphere [31], by taking advantage of synergetic coupling effects or doping with foreign transition metal and non-metal atoms (for example, Fe, Co, Cu, N, P, O and Ni) into MoS_2 to increase the number of unsaturated atom sites along the MoS_2 edges. These schemes further help in modifying the electronic properties of MoS_2 and enhance the intrinsic conductivity [32-35]. Engineering of interlayer spacing could be a distinct parameter of MoS_2 nanosheets, which has been overlooked as one of the important aspects for tuning properties of MoS_2. Also, interlayer engineering of MoS_2 nanosheets could play a key role in improving their efficacy for energy conversion and storage [36-38]. Expanded interlayer spacing not only significantly improve diffusion kinetics of ions but also enhances the surface area, increase surface catalytically active sites, and reduce diffusion barriers (in particular, when ions with large sizes and multiple valences (Mg^{2+}, Na^{+}) got intercalated between the MoS_2 nanosheets) [36, 39]. Furthermore, expanded interlayer spacing in MoS_2 drastically influences the electronic structures of individual MoS_2 monolayers, specifically, exposing the atoms at the edge-sites, which is essential for catalyzing hydrogen evolution reaction (HER) [40]. Density Functional Theory (DFT) calculations illustrated that even a small interlayer expansion of MoS_2 to 6.57 Å (i.e., 6% interlayer expansion) can reduce the Gibbs free energy of hydrogen adsorption (ΔG_H) by ≈ 0.05 eV [41]. Larger interlayer expansion from 6.2 to 9.5 Å (i.e., 53% interlayer expansion) in MoS_2 further lowers ΔG_H by 0.149 eV [42]. Xie et al. demonstrated oxygen intercalated MoS_2 with an enlarged interlayer spacing of 9.5 Å prepared by a one-pot hydrothermal

method [43]. With additional exposure of active edge sites for HER, the highly active HER catalysts showed an excellent activity with Tafel slopes of 55 mV/dec with a much lower onset overpotential (η) value of 120 mV as well as good long-term stability [43]. Gao et al. reported that the microwave-assisted MoS_2 synthesis process, which increases interlayer spacing up to 9.4 Å results in reducing the Tafel slope to 49 mV/dec and lowering the onset potential to 103 mV for HER [44]. Attanayake et al. reported the sodium ion (Na^+) intercalation into the MoS_2 with 12.33 Å interlayer spacing exhibiting the low overpotential (η=183 mV) and small Tafel slopes of 45 mV/dec [45]. Wang et al. reported ammonia (NH_3^+) intercalated MoS_2 film with enlarged interlayer spacing, which also improved the HER with a smaller Tafel slope (49 mV/dec) and low overpotential [8]. Despite such striking approaches, many practical challenges still remain to improve the catalytic activity and stability of 2D-MoS_2 based catalysts for HER.

The reactivity, stability, and electronic properties of MoS_2 can also be modified with the covalent functionalization of the basal site [46, 47]. Recently, Vedhanarayana et.al synthesized the n-Butyle covalent functionalized to 1T-MoS_2 nanosheets and their results show that MoS_2 was still in the metallic 1T phase after the functionalization and improved the electrochemical activity and stability [48]. Similarly, Benson et al. reported the covalent functionalization of 1T-MoS_2 nanosheets with the electron-donating functional group of (p-$(CH_3CH_2)_2$ NPh), which directly influence the kinetics of HER, stability, and surface energetics [49].

To this end, functionalization of S-Mo-S layers with a large molecule could have a better choice to enlarge the interlayer distances of MoS_2, modify the electronic structure, and improve the stability of electrocatalytic activities. Sulfonic (-SO_3H) molecules are unique since they can hybridize with the *p* and *d* states of the S and Mo of the S-Mo-S layers, thus increasing the interlayer distances of MoS_2 and changing electronic structures by shifting the

valance band maxima (VBM); thereby improving the carrier concentrations in MoS_2 structure. Interestingly, $-SO_3H$ functional group is stable in water as well as non-oxidizing, thus, could offer faster charge transfer with enhanced stability to the structure while enhancing the HER via water splitting.

In this work, we have developed in-situ functionalization of MoS_2 with sulfonic ($-SO_3H$) group via one-pot hydrothermal synthesis followed by characterizing the MoS_2 structure and structure-function relationship using X-ray diffraction (XRD), Transmission electron microscopy (TEM), Fourier transforms infrared spectroscopy (FTIR), X-ray photoelectron spectroscopy (XPS), Raman spectroscopy, and electrochemical methods. We used the SO_3H-MoS_2 as electrocatalytic electrodes for HER and found the enhanced charge-transfer kinetics in functionalized MoS_2 compared to the pristine one. We have also demonstrated the step-by-step controlled functionalizations by changing the molar ratios to the saturation where we found enhanced electrocatalytic performance. The DFT calculations showed that the sulfonic group is adsorbed on the surface of MoS_2 via the charge distribution wherein the surface Mo atom loses, and S atoms gain charge. There is a charge distribution between the S, O, and H atoms, thereby making the functional group stable and attaches to the surface.

5.2 Results and discussions

In-situ $-SO_3H$ functionalized MoS_2 was synthesized by a one-pot hydrothermal method at 180 ^oC in a hot air oven, as discussed in the experimental section 2.1.8 of chapter 2. In the typical process, we have synthesized 2D-MoS_2 nanosheets by taking 2.067 g of ammonium molybdate tetrahydrate $(NH_4)_6Mo_7O_{24}.4H_2O$ while increasing thiourea (CH_4N_2S) to molar ratios of 2, 4, 6, 8, and 10. These samples were addressed as MoS_2-2, MoS_2-4, MoS_2-6, MoS_2-8, and MoS_2-10 during all experimentation and data analysis.

As a mechanism of functionalized MoS_2 synthesis, we believe that thiourea hydrolysis play key role as given in Equation 5.1 and Equation 5.2. Where thiourea (CH_4N_2S) undergoes various dissociation and decomposition reactions and transformed into S^{2-} anion via the hydrolysis step at the elevated temperature.

$$(NH_2)_2CS + 2H_2O \rightarrow 2NH_3 + CO_2 + H_2S \quad (5.1)$$

$$H_2S + 2OH^- \rightarrow S^{2-} \quad (5.2)$$

Ammonium heptamolybdate tetrahydrate $(NH_4)_6Mo_7O_{24}$ was reduced at elevated temperature by the following reaction (Equation 5.3 to 5.5).

$$(NH_4)_6Mo_7O_{24}.\ 4H_2O \rightarrow 6NH_3 \uparrow + 7MoO_3 + 7H_2O\uparrow \quad (5.3)$$

$$MoO_3 + 3\ S^{2-} + H_2O \rightarrow MoO_2 + SO^{2-}_4 \quad (5.4)$$

$$MoO_2 + S^{2-} \rightarrow MoS_2 \quad (5.5)$$

With increasing the thiourea precursor content, S^{2-} anion concentration is increased in the aqueous medium. This leads to the functionalization of the sulfonic ($-SO_3H$) group on MoS_2.

Comparative Raman spectra in Figure 5.1 show two characteristic peaks at ~374 cm^{-1} and ~401 cm^{-1} for each sample associated with the in-plane vibration of E^1_{2g} and out of plane vibration of A_{1g} mode of MoS_2 bands [50]. In the in-plane mode, the sulfur (S) and molybdenum (Mo) atoms vibrate in two opposite directions within the layer plane. In contrast, in the out-of-plane mode, only sulfur (S) atoms vibrate in the one vertical direction of the plane [51]. The differences between the two modes (A_{1g} - E^1_{2g} = Δk) typically determine the number of MoS_2 layers formed during the hydrothermal synthesis as shown in Table 1 [52]. When the thiourea molar ratio is increased, the second-order Raman scattering peaks observed at ~449.2 cm^{-1}, ~585.5 cm^{-1}, ~746.79 cm^{-1}, and ~816.87 cm^{-1} are corresponding to the 2LA, E_{1g}, $2E_{2g}$, and A_{1g} modes of vibration occurring due to the

coupling of phonon mode to electronic states existed optically in the crystals [53]. Raman peak at ~1013 cm^{-1} in MoS_2-6, MoS_2-8, and MoS_2-10 corresponds to the -SO_3H group and manifests that increasing the CH_4N_2S molar ratios to 6, 8, and 10, the -SO_3H functionalizations occurred [54].

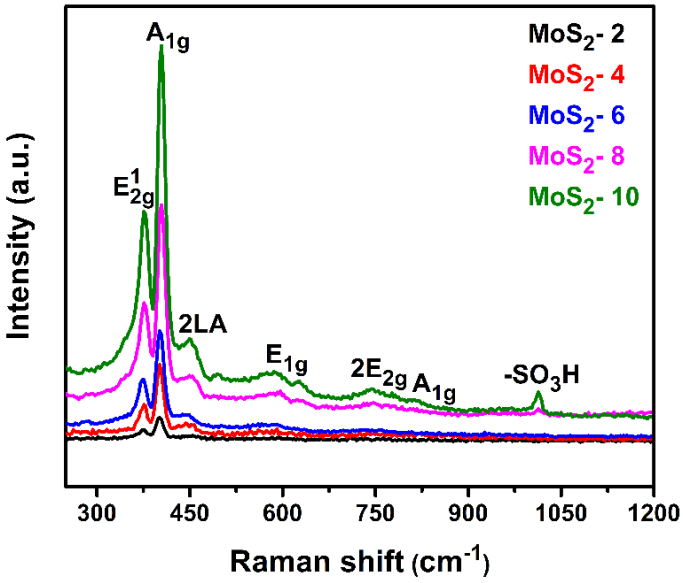

Figure 5.1: *Comparative* Raman *Spectra of all as-synthesized MoS_2 samples with the different molar ratios of thiourea.*

Table 5.1: Lists the Raman peak positions of various MoS_2 samples

Sample	E^1_{2g} (cm^{-1})	A_{1g} (cm^{-1})	Δk (cm^{-1})
MoS_2 -2	374.82	401.33	26.5
MoS_2 -4	377.30	401.75	24.4
MoS_2 -6	374.82	402.16	27.3
MoS_2 -8	377.33	404.26	26.9
MoS_2 -10	377.75	404.67	26.9

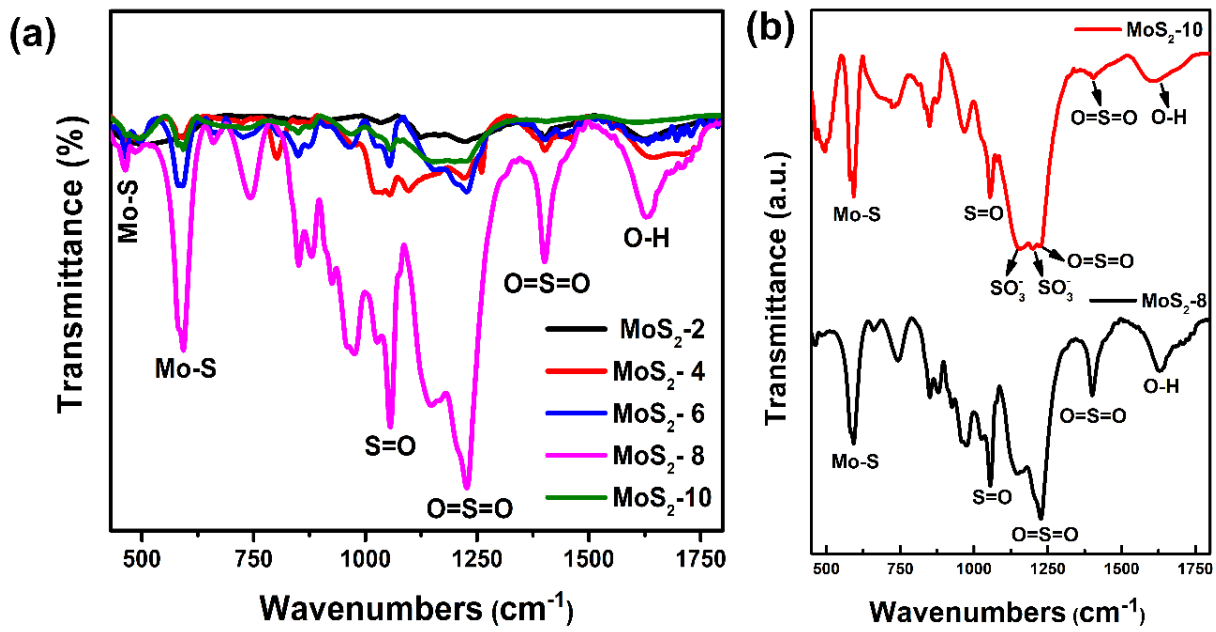

Figure 5.2: Shows *(a) comparative Fourier transform infrared (FTIR) spectra of all pristine and functionalized MoS_2 sample; (b) A comparative FTIR spectra of MoS_2-8 and MoS_2-10.*

The Fourier transform infrared (FTIR) measurement was carried out to obtain the bending and stretching vibration of the functional group present in the as-synthesized all MoS_2 samples (Figure 5.2a). The broad absorption bands at ~1627 cm^{-1} (O-H) are associated with the surface absorbed water molecule [55]. Two absorption bands at ~462 cm^{-1} and ~594 cm^{-1} are corresponded to the Mo-S stretching vibration [56, 57]. Absorption bands observed at 1056 cm^{-1} is associated with the S=O (SO_3^-) stretching mode of -SO_3H functional group [58-60]. Two absorption bands at 1227 cm^{-1} and 1402 cm^{-1} are associated with the O=S=O stretching mode of the -SO_3H functional group [61-63]. When thiourea molar ratio increased from MoS_2-8 to MoS_2-10 in Figure 5.2b we observed that there is a successive transformation of the SO_3^- group along with the -SO_3H functional group [63]. The FTIR spectrum indicates that the as-prepared MoS_2 sample exhibits the Mo-S bands. The formation of the -SO_3H group (S=O and O=S=O) signifies the functionalization of the -SO_3H functional group on the surface of MoS_2 nanosheets.

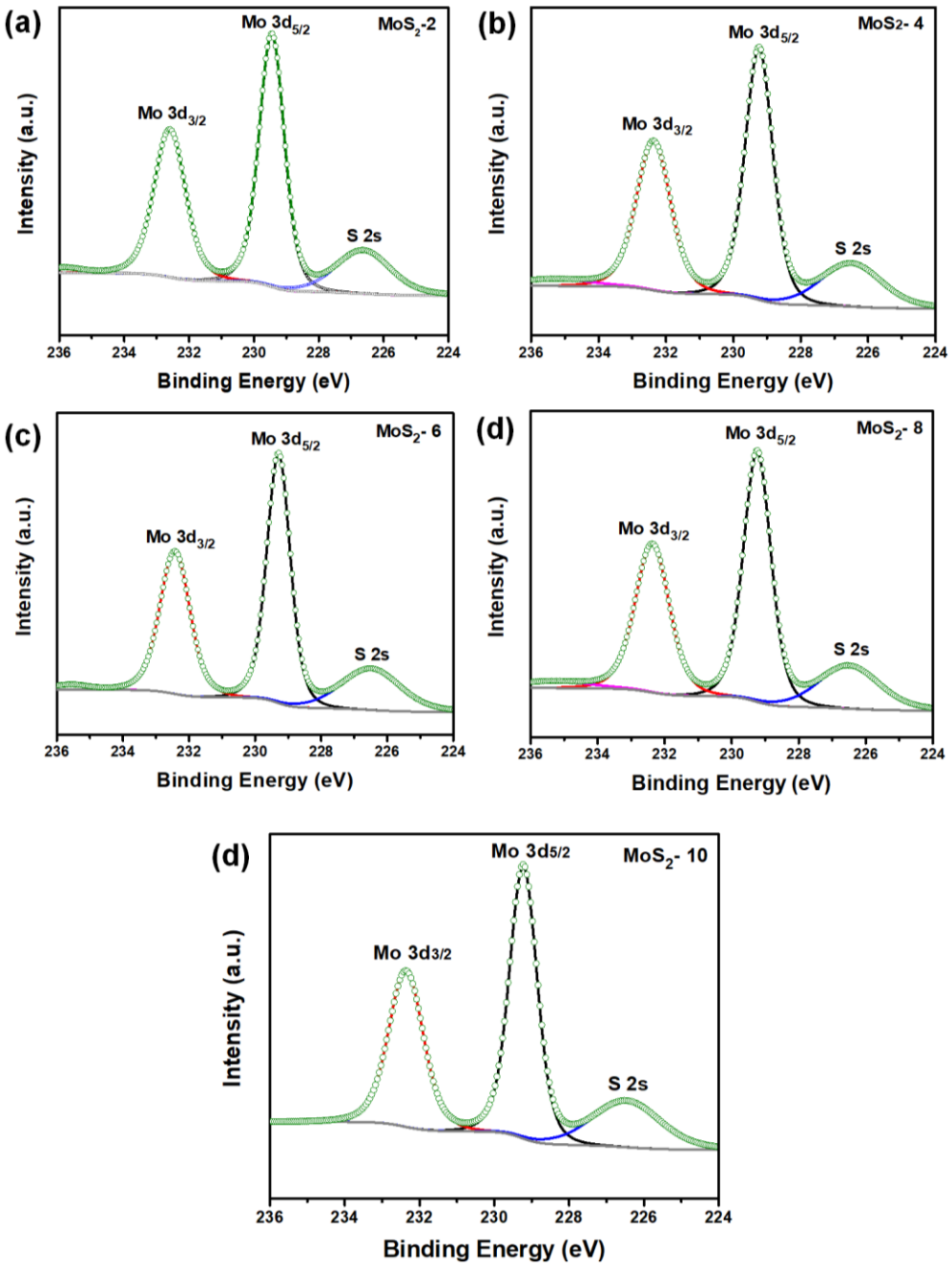

***Figure 5.3**: High-resolution Mo 3d XPS spectrum of all as-synthesized MoS_2 nanosheets with varying molar ratios of thiourea. The entire XPS spectrum was analyzed by the CasaXPS software. The two characteristic peaks Mo $3d_{5/2}$ and Mo $3d_{3/2}$ located at ~229.17±0.28 eV and ~232.32±0.28 eV correspond to the Mo^{4+} oxidation states, while the peak located at ~226.40±0.25 eV to S 2s in MoS_2.*

XPS data shows the chemical composition and valency states of all the elements in samples, as shown in Figure 5.3 and Figure 5.4. The high-resolution Mo 3d XPS (Figure 5.3 a-e) spectrum can be deconvoluted into three peaks. The characteristic peaks Mo $3d_{5/2}$ and Mo $3d_{3/2}$ were found located at ~229.17±0.28 eV, and ~232.32±0.28 eV correspond to the Mo^{4+} oxidation states, while the peak obtained at ~226.40±0.25 eV represents S 2s in MoS_2 (as listed in Table 5.2) [64]. In the high-resolution S 2p XPS, Figure 5.4 a_1-e_1 spectra show two pairs of S $2p_{3/2}$ and S $2p_{1/2}$ spin-orbit doublets. The XPS peaks at 162.02±0.26 eV and 163.24±0.21 eV represent the S $2p_{3/2}$ and S $2p_{1/2}$ binding energy of S^{2-}, respectively [65]. In the high-resolution S 2p XPS, Figure 5.4 a_1-e_1 spectra show two pairs of S $2p_{3/2}$ and S $2p_{1/2}$ spin-orbit doublets. The XPS peaks at 162.02±0.26 eV and 163.24±0.21 eV represent the S $2p_{3/2}$ and S $2p_{1/2}$ binding energy of S^{2-}, respectively [65]. The XPS peaks at higher binding energies of (Figure 5.4 c_1 and Figure 5.4 d_1) ~168.57±0.19 eV and ~169.12±0.14 eV confirm the presence of S $2p_{3/2}$ and S $2p_{1/2}$ of S-OH and S=O obtained from the -SO_3H functionalized MoS_2 as listed in Table 5.2 [63, 66]. In MoS_2-10 sample (Figure 5.4 e_1), XPS peak observed at 166.6 eV, which is corresponding to the SO_3^- functional group along with the two successive peaks of -SO_3H group at 168.80 eV (S $2p_{3/2}$) and 169.8 eV (S $2p_{1/2}$). This result further suggests that when we increased the thiourea molar ratios from MoS_2-8 to MoS_2-10, there is the formation of the SO_3^- functional group along with the -SO_3H functional group in MoS_2-10 sample. Similarly, Figure 5.4 a_2-e_2 demonstrates the high-resolution deconvolution of O1s XPS spectra. In Figure 5.4 c_2-e_2 depicts two oxygen peaks at ~532.20±0.63 eV, and ~533.16±0.47 eV correspond to the S-OH and S=O, respectively [59, 67]. The further details of all the XPS peaks and their positions as listed in Table 5.2.

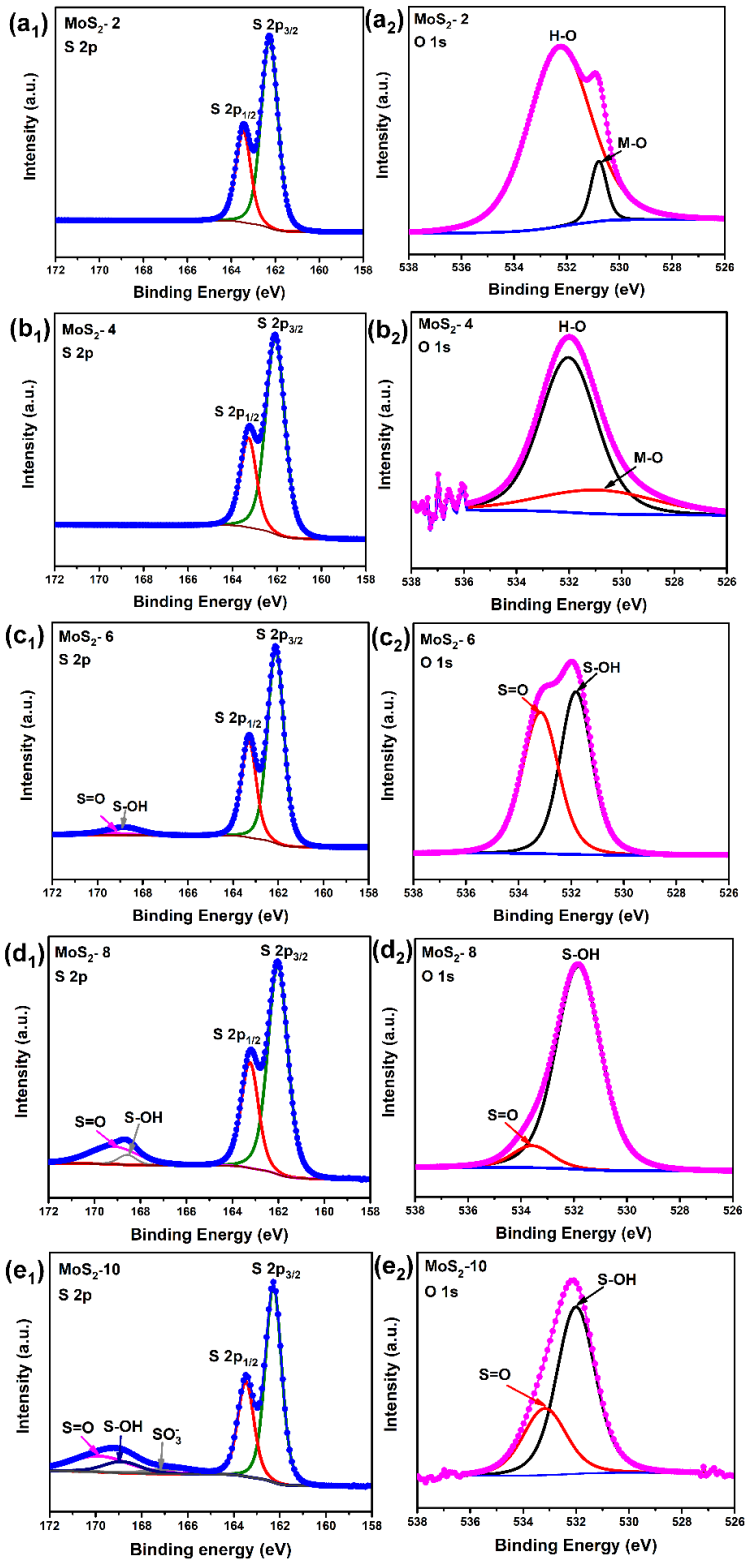

Figure 5.4: *(a_1-e_1) Comparative S 2p and (a_2-e_2) O1s peak obtained from X-ray photoelectron spectroscopy of as-synthesized MoS_2 nanosheets with varying molar ratios of thiourea.*

We observe that with the molar ratios of $(NH_4)_6Mo_7O_{24}.4H_2O$ and CH_4N_2S as 1:2, and 1:4, the 2D-MoS_2 turns out to be pristine. However, after increasing the thiourea molar ratios to 1:6, 1:8, and 1:10, the sulfonic group starts forming, and the functionalized MoS_2 nanosheets are produced. The percentages (%) of functional groups are 1.47, 4.84, and 3.45%, with respective molar ratios of 1:6, 1:8, and 1:10. We believe that the formation of MoS_2 during the hydrothermal process involves various intermediated stages, where MoO_3 and MoO_2 form first, followed by the transformation of Mo-oxides into 2D-MoS_2 nanosheets in the presence of H^+ and SO_4^- ions in the solution [68-71]. With increasing the thiourea content the excess SO_4^- ions get attached to the MoS_2 surface as well as intercalated through the 2D-MoS_2 interlayers, thereby produced the -SO_3H functionalized 2D-MoS_2 nanosheets.

Table 5.2: Demonstrates XPS peak parameters for all MoS_2 samples

	Mo 3d (eV)		**S 2p (eV)**					**O 1s (eV)**				
Sample	**$3d_{5/2}$**	**$3d_{3/2}$**	**S 2s**	**$2p_{1/2}$**	**$2p_{3/2}$**	**S-OH**	**S=O**	**SO_3**	**M-O**	**H-O**	**S-OH**	**S=O**
MoS_2-2	229.45	232.59	226.62	162.26	163.45	-	-	-	530.79	532.27	-	-
MoS_2-4	229.24	232.37	226.46	162.07	163.28	-	-	-	530.88	532.02	-	-
MoS_2-6	229.29	232.42	226.48	162.11	163.30	168.76	169.26	-	-	-	531.82	533.16
MoS_2-8	229.17	232.32	226.40	162.02	163.24	168.57	169.12	-	-	-	532.83	533.58
MoS_2-10	229.45	232.60	226.65	162.28	163.47	168.80	169.80	166.6	-	-	532.20	533.18

The crystal structure and phase purity of all 2D-MoS_2 nanosheets were analyzed by the X-ray diffraction (XRD) method, and comparative XRD plots for all the samples were presented in Figure 5.5. In pristine MoS_2, (i.e., sample MoS_2-2, the red curve in Figure 5.5) diffraction peaks were obtained at 14.23º, 33.62º, 39.78º, and 58.95º, which corresponds to crystal planes

of (002), (010), (013), and (110) of 2D-MoS_2. The (002) peak at 14.23º corresponds to the MoS_2 interlayer distance of 6.2 Å. It was observed that with increasing the molar ratios of thiourea (from 2 to 10), the successive shifts of the (002) plane occurred corresponds to the increase of the interlayer spacing of as-synthesized 2D-MoS_2 nanosheets. For example, in MoS_2-4 (the blue curve in Figure 5.5), most of the diffraction peaks were shifted to the lower angle side at 2θ=14.03º, 33.47º, 39.72º, and 58.87º, which are attributed to the MoS_2 crystal planes with the successive increase in the interlayer distance (i.e., for (002) plane it is 6.3 Å). When the thiourea molar ratio was further increased from 4 to 6 (green curve), (002) peak of MoS_2 is shifted to the further lower angle where two new peaks emerged at 9.43º (002) and 17.98º (004), and the equivalent d-spacing was found to be 9.4 Å and 4.92 Å, respectively. The diploid relation between the d-spacing indicated the formation of a new lamellar structure with the enlarged interlayer d-spacing of 9.4 Å [48]. Moreover, two peaks at higher angles at 32.64º and 57.68º correspond to the (010) and (110) crystal planes of the MoS_2, indicating that the MoS_2 crystal structure remains the same even after the -SO_3H functionalization. Similar trends were observed in MoS_2-8 and MoS_2-10 (yellow-green and pink curves, respectively) with the successive lower angle shift in the XRD data. It may be presumed that in -SO_3H functionalized MoS_2, a certain -SO_3H molecules were intercalated through the 2D MoS_2 interlayers, thereby emerging as functionalized MoS_2 nanosheets (for MoS_2-6, MoS_2-8, and MoS_2-10) with enlarged interlayer distances. Thus, it can be inferred that the attachments of the -SO_3H group occurred on MoS_2 simultaneously via surface hybridization as well as intercalation, which will be discussed further in the next sections (XRD and TEM/HRTEM).

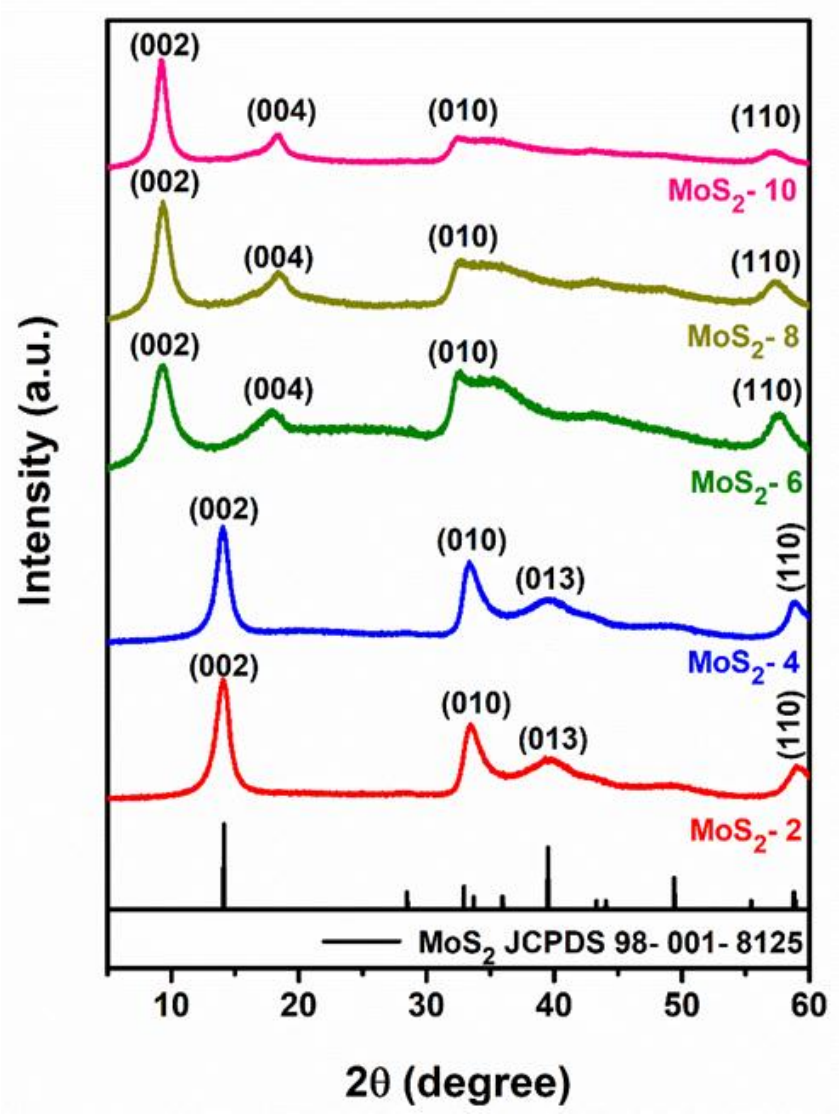

Figure 5.5: *Shows a comparative XRD plots of all as-synthesized MoS_2 nanosheets with varying molar ratios of thiourea compared with MoS_2 (JCPDS # 98-001-8125).*

Scanning electron microscopy was used to characterized morphology and the structure of as-synthesised 2D-MoS_2 and functionalized MoS_2 as shown in the Figure 5.6. It seems the as-synthesised 2D-MoS_2 consist of petal-like nanosheets, which are agglomerated and bind together to from the flower like nanostructure. The 2D-MoS_2 nanosheets exhibit sharp edges, which play a key role in faster electron transfer for higher catalytic activity as discussed in the electrochemical sections. However, it was noticed that the primary nano-flower structure

of 2D-MoS_2 remain same even after the sulphonic acid (SO_3H) functionalization (Figure 5.6 d_1-d_2 and Figure 5.6 e_1-e_2).

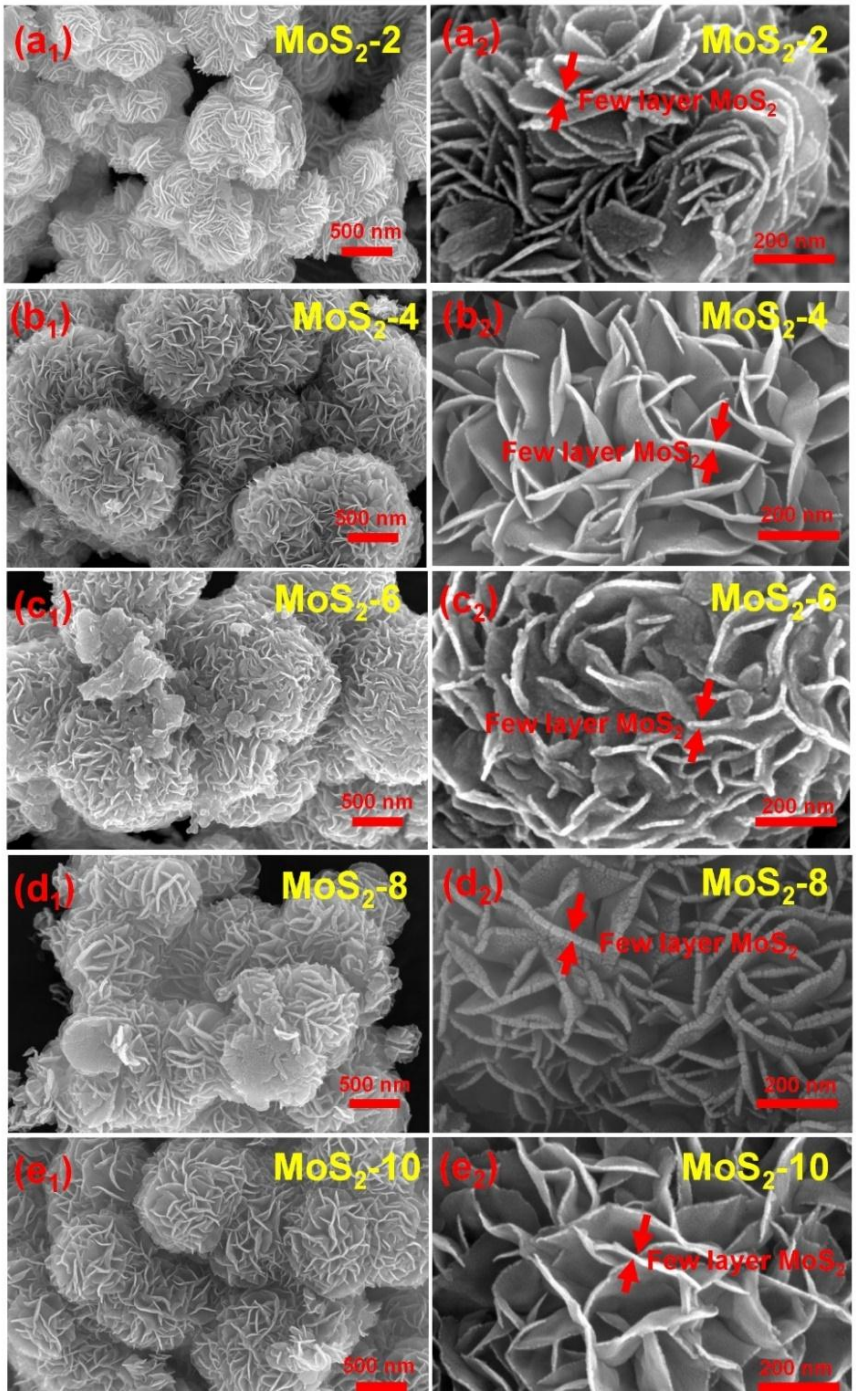

Figure 5.6: *Shows the scanning electron micrographs with different magnifications with scale bars of ~500 nm and ~200 nm, (a_1 and a_2) MoS_2-2, (b_1 and b_2) MoS_2-4, (c_1 and c_2) MoS_2-6, (d_1 and d_2) MoS_2-8 and (e_1 and e_2) MoS_2-10.*

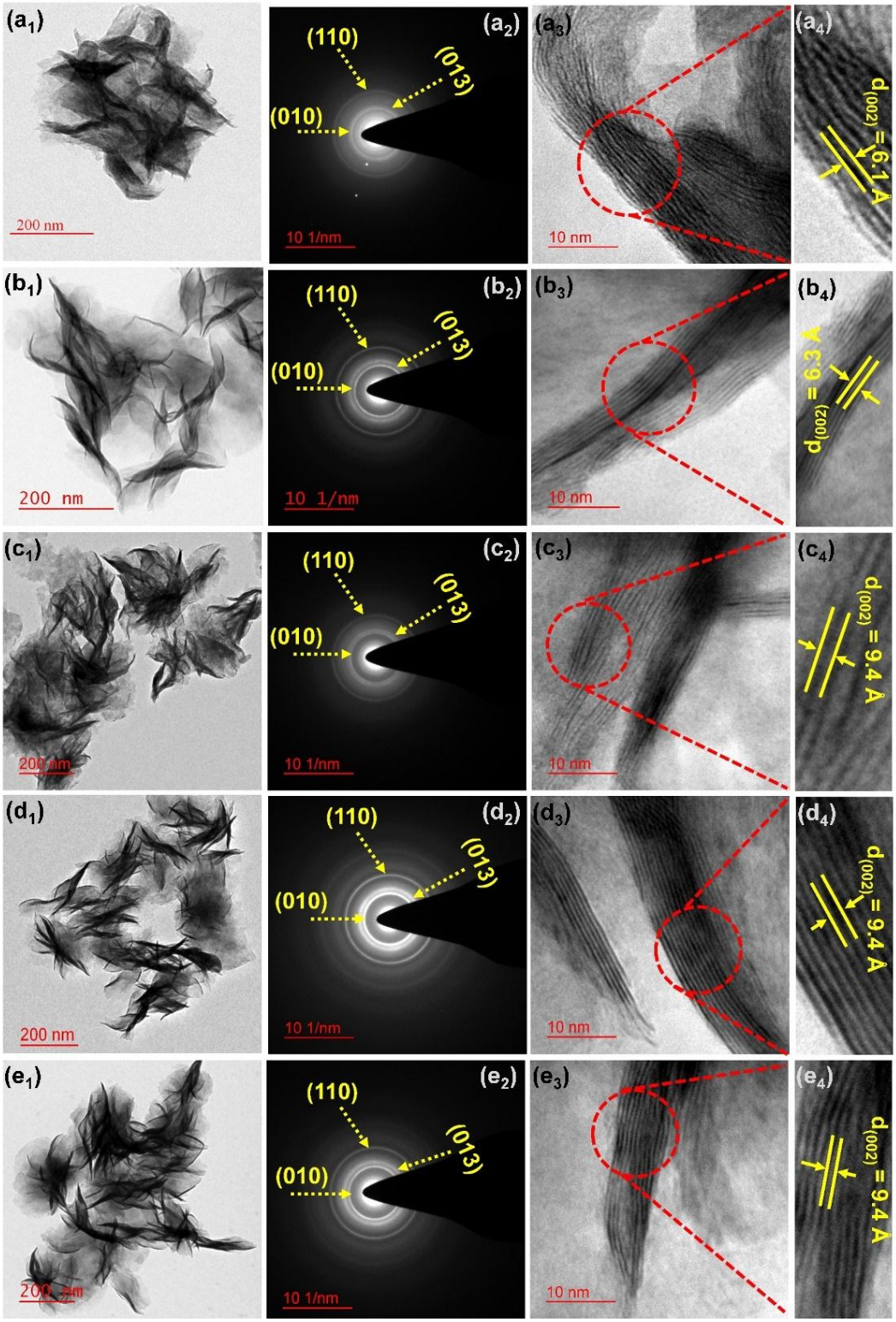

Figure 5.7: *(a_1, a_2, a_3, and a_4) Shows the TEM, SAED pattern, and HRTEM of MoS_2-2 with the interlayer d-spacing of 6.1 Å; (b_1,b_2, b_3, and b_4) TEM, SAED pattern, and HRTEM of MoS_2-4 with the interlayer d-spacing of 6.3 Å; (c_1,c_2, c_3, and c_4) TEM, SAED pattern and*

HRTEM of MoS_2-6 with the interlayer d-spacing of 9.4 Å; (d_1, d_2, d_3, and d_4) TEM, SAED pattern and HRTEM of MoS_2-8 with the interlayer d-spacing of 9.4 Å; and (e_1,e_2, e_3, and e_4) TEM, SAED pattern and HRTEM of MoS_2-10 with the interlayer d-spacing of 9.4 Å.

Figure 5.7 shows the transmission electron microscopy (TEM) and high-resolution transmission electron microscopy (HRTEM) images of all pristine and functionalized MoS_2 samples. Figure 5.7 a_1-e_1 shows transmission electron micrographs of all MoS_2 samples with ultra-thin nanosheets like two-dimensional morphology along with certain ripples and corrugations. All these micrographs show that the structure and morphologies were not changed during the functionalization of 2D-MoS_2 nanosheets. Figure 5.7 a_2-e_2 shows the respective SAED patterns of all MoS_2 samples with the characteristic diffraction planes of (001), (013), and (011), indicating that the MoS_2 crystal structure remains identical even after the -SO_3H functionalization of nanosheets. Slight changes were observed in diffraction rings due to interlayer distances enlargements, specifically for MoS_2-6, MoS_2-8, and MoS_2-10 samples. Figure 5.7 a_3-e_3 shows the high-resolution TEM images of all the samples illustrating the few to multi-layered 2D-MoS_2 nanosheet with lamellar morphologies. Similarly, Figure 5.7 a_4-e_4 shows the magnified images of all MoS_2 samples depicting the crystalline MoS_2 nanosheets with varying interlayer spacing of (002) plane. The (002) interlayer spacing were found increasing successively from 6.1 Å to 9.4 Å in MoS_2-2 to MoS_2-10, respectively, which may be due to the intercalation of -SO_3H ions as discussed in the Raman, FTIR, XPS, and XRD sections earlier.

The thermal stability of SO_3H-MoS_2 was determined by the thermogravimetric analysis (TGA) and differential scanning calorimetry (DSC) analysis as shown in Figure 5.8a. In Figure 5.8a, it can be clearly seen that the endothermic peak (DSC curve, the blue curve) of the -SO_3H group disintegrating from the MoS_2 at T_{max}= 325.6 ^oC. The temperature is associated with a sharp 4.89 % Weight loss in the TGA curve (the black curve in Figure

5.8a). After obtaining the -SO_3H dissociation temperature from DSC/TGA curve, we did the heat treatment of the same sample under identical conditions (inert gas atmosphere) for a certain period (~ 350 ^oC, 2 h). We did the XRD before and after the heat treatment, as shown in Figure 5.8b.

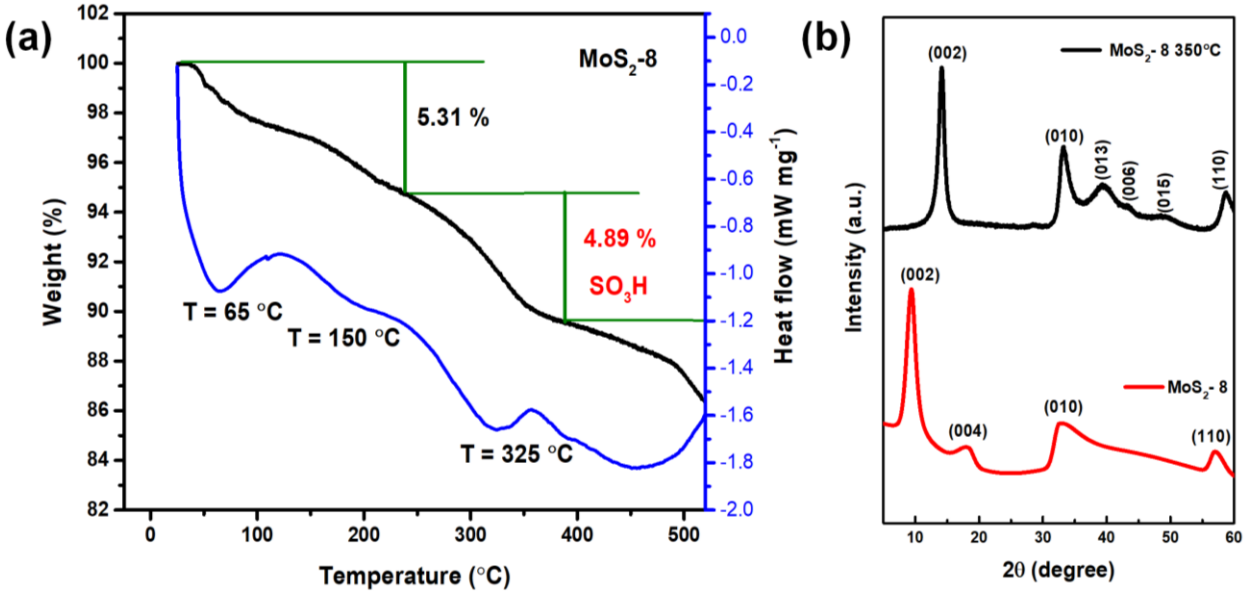

Figure 5.8: *Shows (a) the TGA and DSC curves for MoS_2 -8; (b) shows the XRD pattern of MoS_2-8 before and after the annealing at 350 ^oC for 2h in an inert gas atmosphere.*

Figure 5.8b illustrates that the (002) peak of the MoS_2-8 sample was shifted back to its original position (exactly like the pristine MoS_2-2 sample) from ~ $2\theta = 9.4^o$ ($d_{(002)}$ = 9.4 Å) to ~$2\theta = 14.10^o$ ($d_{(002)}$ = 6.25 Å), which attributed to the de-intercalation of the -SO_3H group out of the (002) plane and restored its original lattice spacing. Again, this was further verified by the HRTEM, which shows the d-spacing is reduced from 9.4 Å (Figure 5.9 d and Figure 5.9 f) to 6.28 Å. All these experimentations demonstrate that the -SO_3H functionalization in 2D-MoS_2 occurred not only at the surface but also at the -SO_3H group intercalated through the inter-planar spacing (i.e., (002) plane) as well.

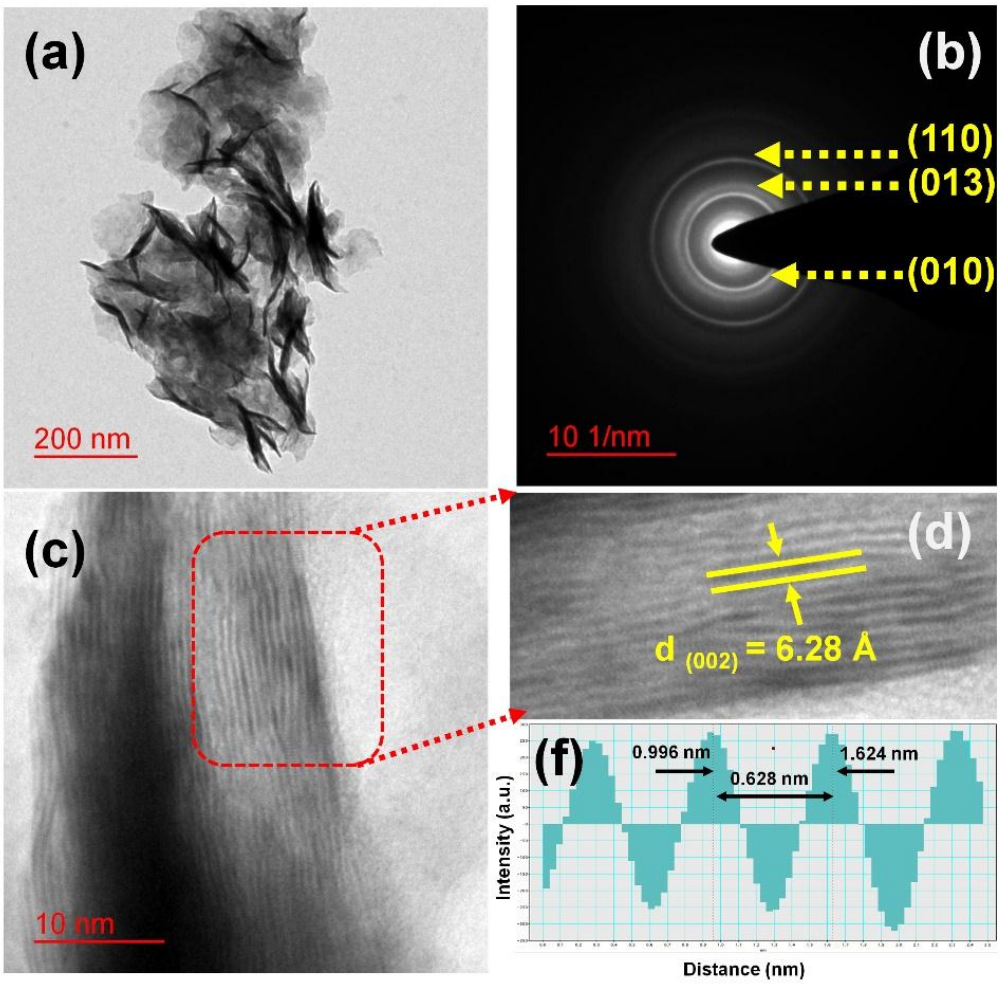

Figure 5.9: *Shows (a) TEM, (b) SAED pattern; (c & d) HETRM of MoS_2-8 sample after annealing at 350 ^oC for 2h in an inert gas atmosphere; (f) the IFFT line profile of MoS_2-8 after annealing with the interlayer d-spacing 6.28 Å.*

Since, we observed the surface properties change via Raman spectroscopy, XPS, we use contact angle measurements (section 2.2.10, chapter-2) of as-synthesised pristine and SO_3H-MoS_2 samples (MoS_2-8) to identify their wettability in aqueous solution. Figure 5.10 shows the wetting properties for a MoS_2-2, MoS_2-4 and MoS_2-8 samples in air by using water contact angle measurement. A decrease in contact angle was observed (Figure 5.10) from pristine MoS_2 to sulphonic acid (-SO_3H) functionalized MoS_2, and hence it was observed that the hydrophilicity of the as-synthesized functionalized MoS_2 increases after the functionalization of sulphonic group into MoS_2.

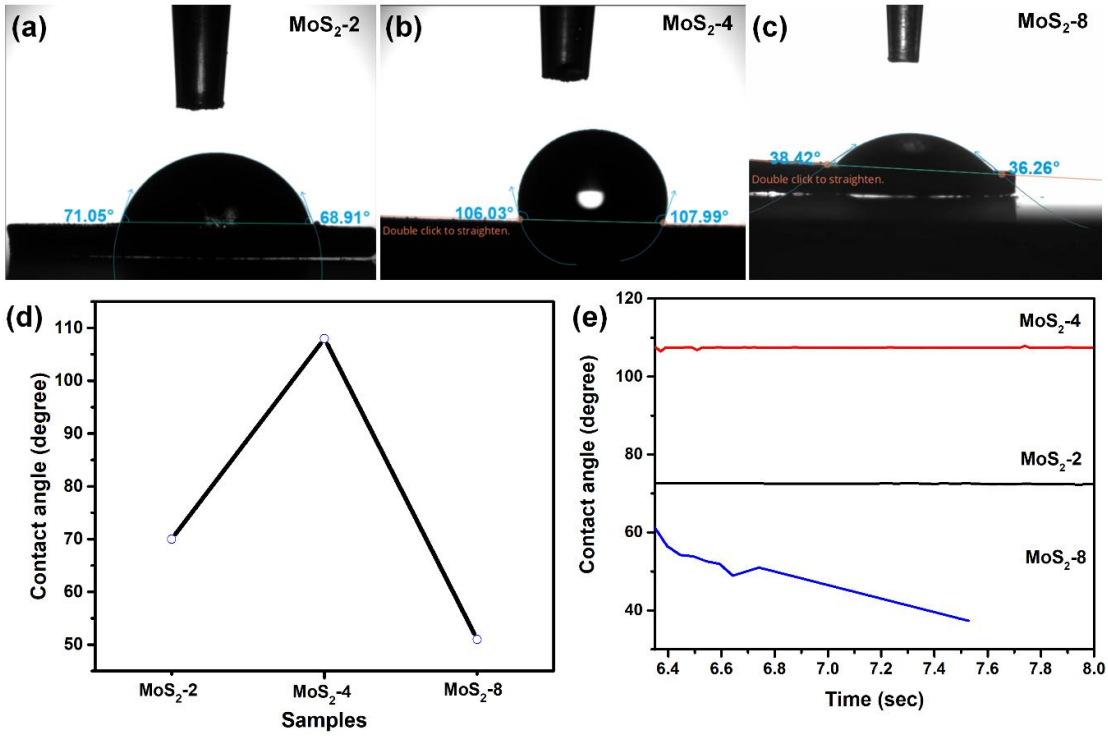

Figure 5.10: *Demonstrates contact angle images of a water droplet on as-synthesised (a) MoS_2-2; (b) MoS_2-4; (c) sulfonic acid (-SO_3H) group functionalized MoS_2 (MoS_2-8); (d) a comparative contact angle data of MoS_2-2 (69°) , MoS_2-4 (106°), and (MoS_2-8 (38°); (e) represents the time dependent dynamic contact angle measurement data showing the lowering of contact angle for MoS_2-8, depicting the improvement in hydrophilicity of the sample.*

All the electrodes for electrochemical studies were fabricated by drop-casting the ink prepared via dispersing as-synthesized powder in isopropanol stabilized with Nafion (5 wt. %) as discussed in section 2.3 of (chapter 2). First, we have investigated the flat band potential (E_{FB}) of the sample by using the Mott-Schottky method. As shown in Figure 5.11 given below, where positive slope of the C^{-2} vs. V plot suggests that the all as-synthesised MoS_2 was *n-type* semiconductor with electron as the majority carriers. The slope of the functionalized MoS_2 is much smaller than the MoS_2-2 to MoS_2-6 nanosheets, showing the high current density in the sulfonic acids functionalized MoS_2. The high current density of

the functionalized MoS_2 plays major role in the enhancement of the electrocatalytic performance. The flat band potential (E_{FB}) was determined from the intersection of the slope with the X-axis of M-S plot (Table 5.3). As shown in the Table 5.3, the flat band potential (E_{FB}) of functionalized MoS_2 nanosheets are more negative than the pristine MoS_2 and MoS_2-6. The upward shift of E_{FB} indicated the more charge transfer to the solid/liquid interface.

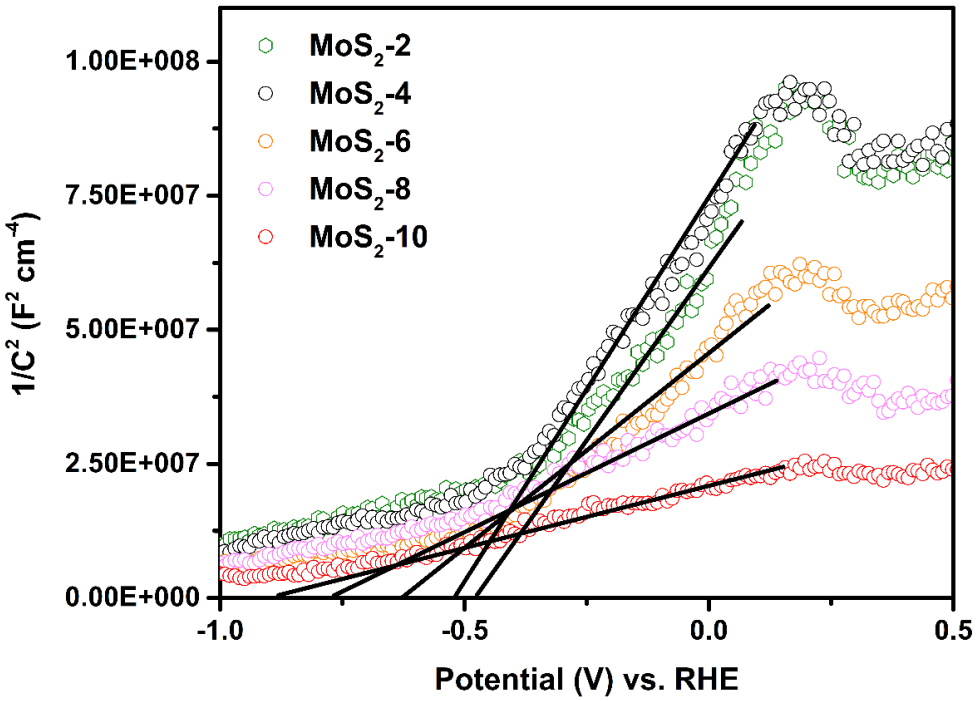

Figure 5.11: *Comparative Mott-Schottky plot of all as-synthesized MoS_2 nanosheets with varying molar ratios of thiourea.*

Table 5.3: Calculated flat band potential (E_{FB}) of as-synthesised pristine and functionalized MoS_2

Sample	Flat band potential (E_{FB})
MoS_2-2	-0.46 V
MoS_2-4	-0.50 V

MoS_2-6	-0.62 V
MoS_2-8	-0.76 V
MoS_2-10	-0.87 V

Furthermore, HER performances of all the as-synthesized MoS_2 and functionalized MoS_2 electrodes were evaluated via series of electrochemical characterizations (as mentioned in detail in the chapter 2 (section 2.3)). Figure 5.12a shows the linear sweep voltammetry (LSV) of the as-prepared MoS_2 catalysts with varying degrees of $-SO_3H$ functionalization with iR corrected with an R (internal resistance. We also performed all the equivalent and similar sets of experiments with graphite paper and commercial Pt wire (99.99% purity) as a reference for this work. Table 5.4 shows the as-calculated electrocatalytic parameters of all MoS_2 samples to demonstrate the HER performances. It can be seen that the overpotential (η_{10}) is linearly decreasing from MoS_2-2 to MoS_2-8 and increasing in MoS_2-10 (277 mV, 188 mV, 139 mV, 82 mV, and 156 mV) where the commercial Pt wire shows low overpotential (η_{10}) ~15 mV, respectively. In this context, graphite paper shows significantly low or no electrocatalytic activity for HER (Figure 5.12a), while Pt wire shows the high electrocatalytic activities as-expected. Among all the MoS_2 samples, the MoS_2-8 catalyst exhibits overpotential (η_{10}) of ~82 mV, which was found lowest than the rest of the other pristine and functionalized electrocatalysts. These results inferred that the MoS_2-8 electrocatalyst shows much superior electrocatalytic performance than the rest of the samples, including, MoS_2-2, MoS_2-4, MoS_2-6, and MoS_2-10.

Figure 5.12b shows that the Tafel slopes of all the as-synthesized samples were derived from the LSV data. The Tafel slope (β) is an inherent property of the catalyst that is determined by the rate-limiting step of the HER. On the surface of electrode, HER mechanisms in alkaline

solution involve two-step processes: (1) electron-coupled water dissociation (Volmer step: $H_2O + e^- = H_{ads} + {}^-OH$, formation of adsorbed hydrogen); (2) The concomitant combination of absorbed hydrogen into molecular hydrogen (I: Volmer- Heyrovsky step: $H_2O + e^- = H_{ads} + {}^-OH$ and $H_{ads} + H_2O + e^- = H_2\uparrow + {}^-OH$ or II: Volmer- Tafel step: $H_2O + e^- = H_{ads} + {}^-OH$ and $H_{ads} + H_{ads} = H_2\uparrow$).[65, 72, 73] It seems that the Tafel slopes (β) decreases with $-SO_3H$ functionalizations from MoS_2-2 (210 $mVdec^{-1}$) to MoS_2-8 (57 $mVdec^{-1}$) as listed in Table 5.4.[74, 75] These successive increases in the electrocatalytic performances as a function of increased % functionalizations may be due to the enrichment in the surface electron concentrations of MoS_2 owing to the hybridizations of $-SO_3H$ to the MoS_2 as discussed in the theoretical section and predicted via DFT calculations.

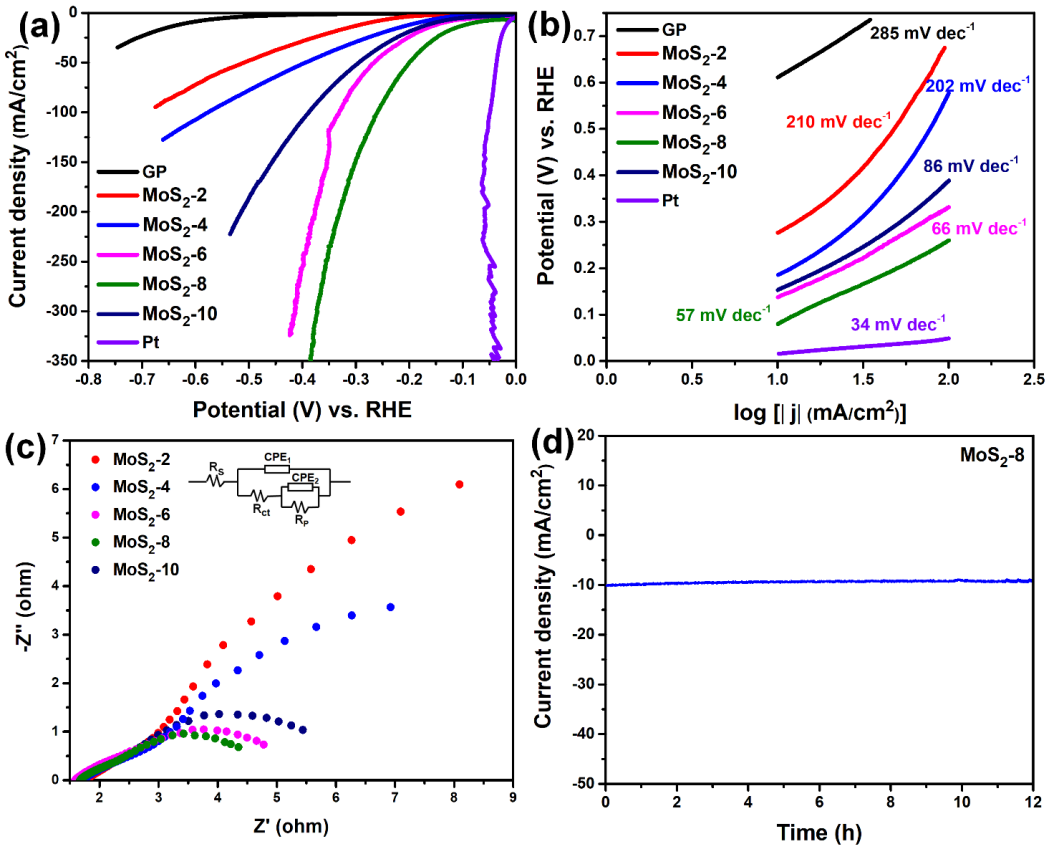

Figure 5.12: *Shows (a) Polarization curve of as-synthesized MoS_2 nanosheets;(b) the corresponding comparative Tafel plot; (c) Nyquist plots; and (d) the stability of the electrode prepared using MoS_2-8 sample.*

It may be consider that the enhancement in the localized electron concentration due to functionalization further leads to the enhancement in the charge-transfer during the electrocatalytic process, which resulted in the low Tafel slope.[48, 76] Likewise, it can be noticed that after MoS_2-8 the Tafel slope for MoS_2-10 started decreasing, which may be due to the rate limiting charge-transfer process occurred owing to the saturation of the -SO_3H functional groups in MoS_2 structure as delineated previously in Raman, FTIR, XPS, XRD, and TEM data. Low Tafel slope and high HER performance of the commercial Pt wire (β = 34 mV dec^{-1}) exhibited due to the low energy barrier (ΔG (H_2O) = 0.44 eV) of the Volmer step provide the Pt catalyst with a faster Tafel step (i.e., Volmer-Tafel step) in alkaline electrolytes.[77] In particular, the -SO_3H functionalized MoS_2 catalyst (MoS_2-8) shows the Tafel slope as low as ~57 mV dec^{-1} (i.e., close to Pt-metal wire itself) compared to the other pristine and functionalized samples, suggesting a coupled Volmer-Heyrovsky type mechanism is followed for HER in this catalyst electrodes.[65, 78].

Table 5.4: Lists HER performances of all MoS_2 electrocatalyst in 1M KOH solution

Sample name	**Ƞ (mV) at 10 mA/cm^2**	**β (mV dec^{-1})**	**C_{dl} (F/cm^2)**
Graphite paper	612	285	-
MoS_2-2	277	210	0.075
MoS_2-4	188	202	0.083
MoS_2-6	139	66	0.108
MoS_2-8	82	57	0.129
MoS_2-10	156	86	0.095
Pt	15	34	-

Electrochemical impedance spectroscopy (EIS) was performed to understand the electrode/electrolyte interface kinetic in the HER process at open-circuit voltage. Figure 5.12c shows the Nyquist plots of all MoS_2 samples, and the Randles equivalent circuit (inset of Figure 5.12c) is used for fitting the EIS experimental results. In the Randles circuit, the capacitor was replaced with a constant phase element (CPE), a typical characteristic of a coated thin-film electrode. Specifically, the CPE represents some distinctive non-ideal/leaky capacitor characteristics of electrocatalytic electrodes. Simultaneously, R_s, $R_{ct,}$ and R_p represent the solution resistance, charge transfer resistance, and absorption resistance, respectively.[25] The R_s, R_{ct}, and R_p values were derived from the EIS fittings of the Randles circuit, as demonstrated in Table 5.5. The MoS_2-8 catalyst shows a much smaller charge transfer resistance (R_{ct}) and solution resistance (R_s) than the rest of pristine and functionalized samples, indicating the higher catalytic conductivity of the MoS_2-8 catalyst. This is primarily due to the effect of the MoS_2 lattice bounded -SO_3H functional group, which especially offers faster charge transfer kinetics owing to the enhancement in the surface-active sites in functionalized samples. It was found that -SO_3H functional group used to attach to nanosheets via *p* and *d* hybridizations with S and Mo atoms of MoS_2, as discussed in the DFT section of this chapter. It seems such hybridization causes the change in density of states (DOS) of MoS_2 nanosheets via shifting of valence band maximum (VBM) and conduction band minimum (CBM). Such VBM shifts are primarily attributed to the enhancement in the carrier concentrations as well as a reduction in the work function (WF) of functionalized MoS_2 nanosheets by improving the charge-transfer kinetics via electrocatalytically active redox properties. Long-term stability is one of the fundamental criteria to figure out the reliable performance of the catalytic electrodes for HER. Figure 5.12d shows the chronoamperometric *(i-t)* data of MoS_2-8 electrocatalyst (the overall high-performance

catalyst electrode) at constant overpotential 200 mV (vs. RHE) for 12 h at a current density of 10 mA/cm^2 in 1M KOH solution suggesting the excellent stability of the MoS_2-8 electrocatalyst in alkaline solution.

Table 5.5: EIS fitting parameters from the equivalent circuit model for all the samples

Parameter	MoS_2-2	MoS_2-4	MoS_2-6	MoS_2-8	MoS_2-10
R_s (Ω)	1.83	1.75	1.53	1.23	1.65
CPE_1 (S-sec^n)	0.0713	0.438	0.037	0.033	0.057
n_1	0.8	0.8	0.8	0.8	0.8
R_{ct} (Ω)	2.5	1.15	0.82	0.69	1.01
CPE_2 (S-sec^n)	0.0729	0.122	0.181	0.148	0.195
n_2	0.8	0.8	0.8	0.8	0.8
R_p (Ω)	3.70	3.31	2.66	2.37	2.92

Figure 5.13 shows the comparative plot of electrochemical double-layer capacitance (C_{dl}) as a function of the scan rate, measure the electrochemical active surface area (ECSA) of all the samples. The C_{dl} was calculated from the CV curves recorded as a function of scan rates for each catalyst electrode, as shown in Figure 5.13 a-e. The C_{dl} value for pristine catalyst (MoS_2-2) was found to be 0.075 F/cm^{2,} whereas C_{dl} was obtained as 0.129 F/cm^2 for MoS_2-8. It could be observed that MoS_2-8 exhibits the higher C_{dl} value indicating the presence of more catalytically active sites on the catalyst's surface, thereby showing the best electro-catalytically active HER in comparison to the other electrodes. The C_{dl} value was further decreased to 0.095 F/cm^2 for MoS_2-10, suggesting the deterioration in the catalytically active

sites may be due to the transformation of the -SO_3H functional group into SO_3^- functional group as discussed in FTIR, XPS and TEM sections.

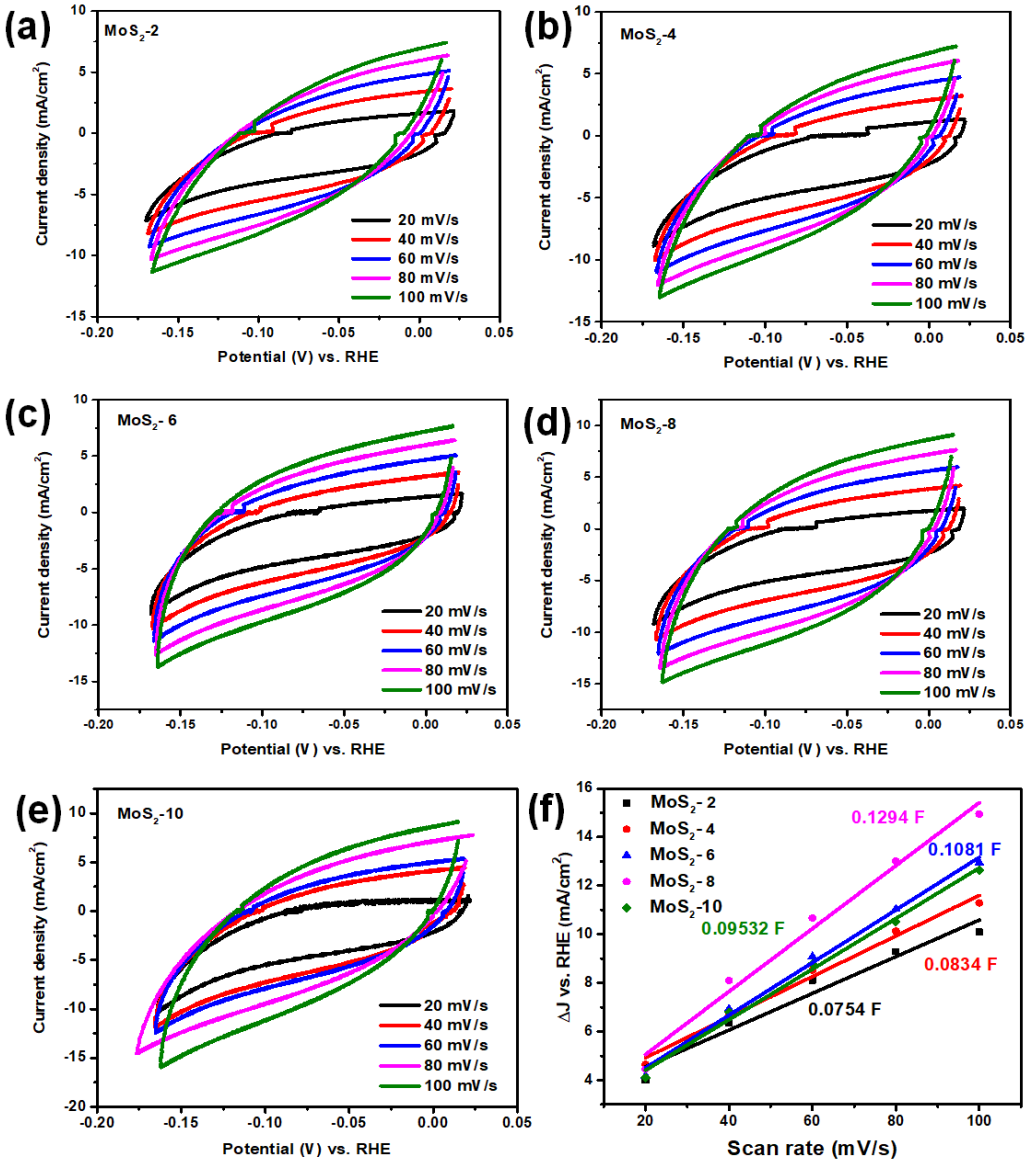

Figure 5.13: *(a-e) Shows the cyclic voltammetry (CV) with different scan rates of 20-100 mV/s for MoS_2 -2 to MoS_2-10; (f) Comparative C_{dl} plot as a function of scan rate.*

Figure 5.14 shows the comparative LSV data of the MoS_2-8 catalyst before and after the stability test demonstrating its reliability performance. We observed that the current density was decreased from 6.5%-7% lowering in current density after 12 h of stability test, and that could be due to the poisoning of the catalytically active sites in MoS_2 nanosheets.[75, 79, 80]

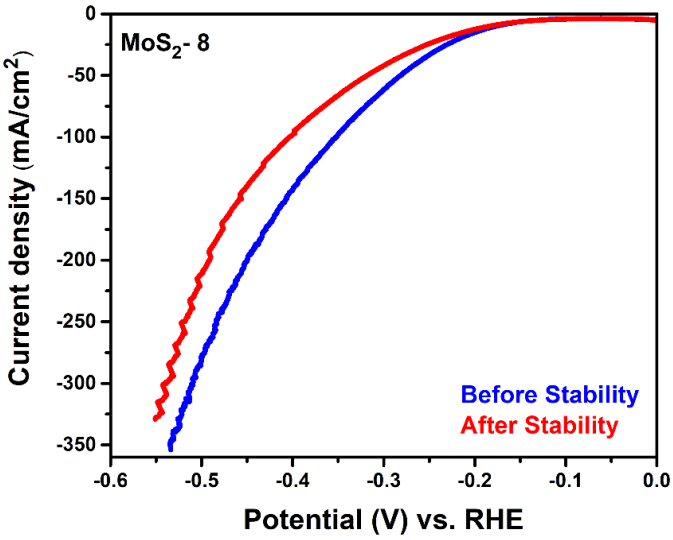

***Figure 5.14**: Comparative LSV data taken before and after the stability test of MoS_2-8 electrode.*

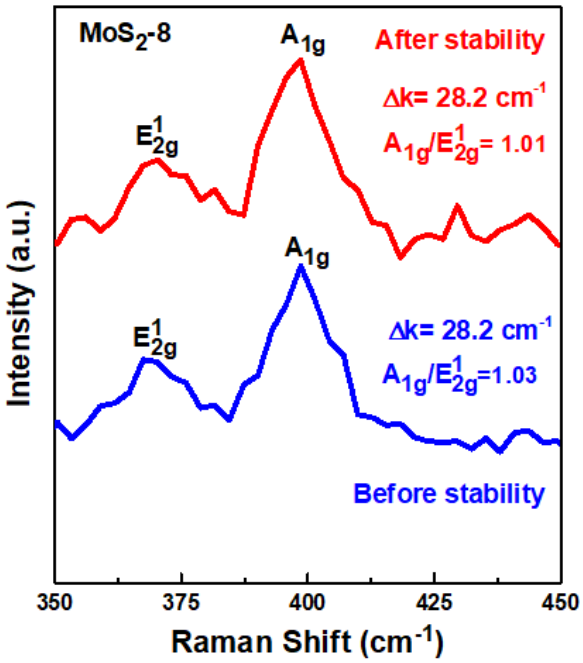

***Figure 5.15:** Comparative Raman spectra of the same electrode taken before and after the stability test showing the characteristics of MoS_2 peaks at the corresponding position ~ 369.7 cm^{-1} (E^1_{2g}) and 398.5 cm^{-1} (A_{1g}) before the stability test while the same position was found at ~ 372.2 cm^{-1} (E^1_{2g}) and 398.5 cm^{-1} (A_{1g}) for the electrode after the*

stability test. In this regard, it should be mentioned that even after the stability test for12h in 1M KOH solution at 10 mA/cm current density, no significant changes in the bonding and structure were observed for the as-functionalized 2D-MoS_2 nanosheets (MoS_2-8) catalyst.

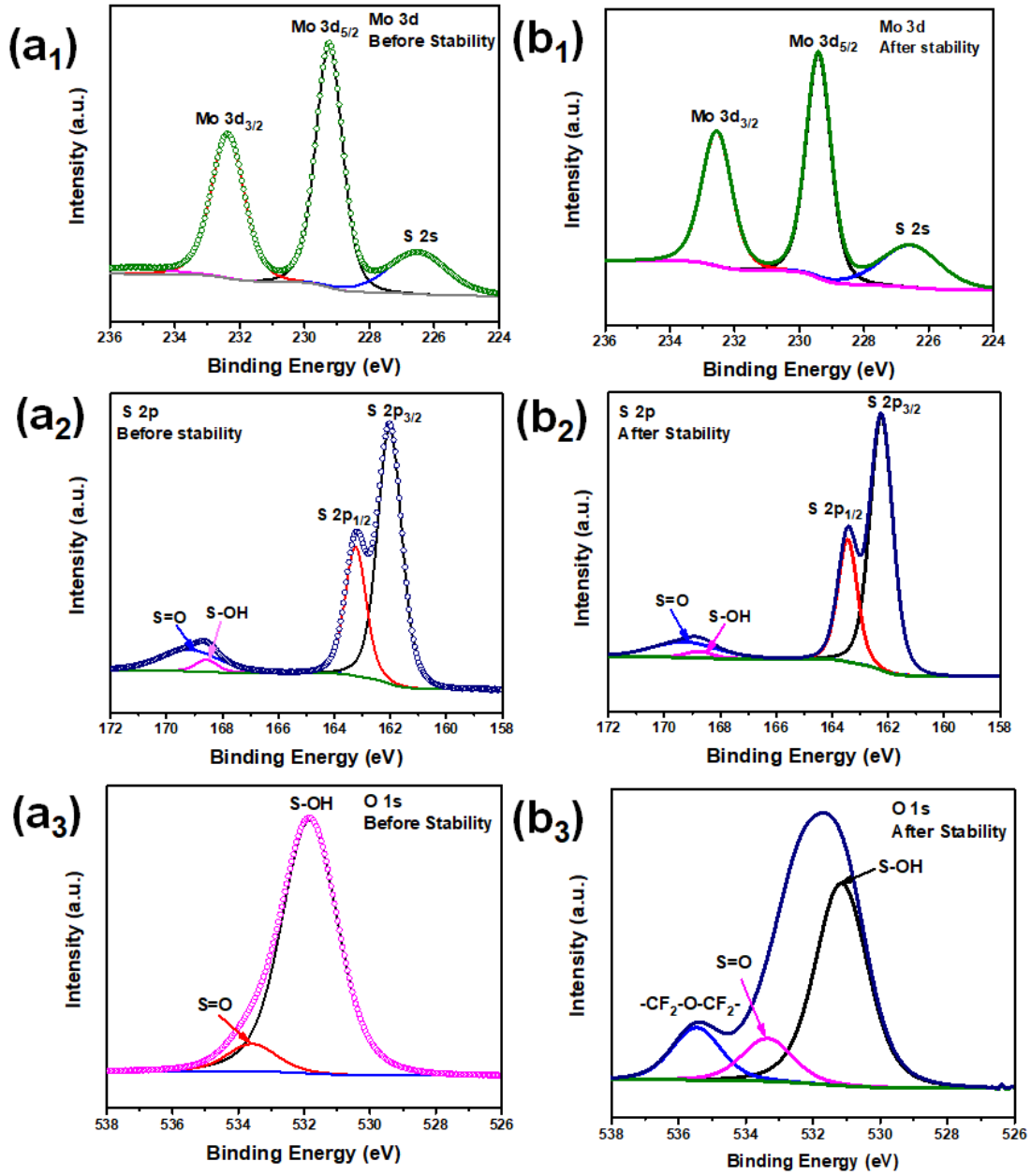

Figure 5.16: *Shows comparative XPS spectra of before and after the 12h stability data of MoS_2-8 samples depicting (a_1-a_2) Mo3d, (b_1-b_2) S 2p, and (c_1-c_2) O1s.*

Figure 5.15 shows the Raman spectrum of MoS_2-8 catalyst electrode before and after the stability test, where it was realized that even after the 12 h stability test, the MoS_2

characteristic Raman peak positions, peak intensity ratios, and Δk values change negligibly, suggesting the development of highly stable structure of -SO_3H functionalized MoS_2 electrocatalysts for HER. Furthermore, Figure 5.16 depicts the XPS spectra of the same (MoS_2-8) catalyst electrode after the stability test. In Mo 3d spectrum, the two characteristic peaks Mo $3d_{5/2}$ and Mo $3d_{3/2}$ located at ~229.41 eV and ~232.55 eV correspond to the Mo^{4+} oxidation states and the peak at ~226.56 eV represents the S 2s binding energy in MoS_2. The S 2p XPS spectrum shows two pairs of S $2p_{3/2,}$ and S $2p_{1/2}$ spin-orbit doublets at 162.24 eV and 163.45 eV represent the S 2s in MoS_2, respectively. The XPS peaks at higher binding energies ~168.76 eV and ~169.27 eV confirm the existence of S-OH and S=O bonds as obtained earlier during the before stability test (Figure 5.16a_2). This further ensures that the -SO_3H functional group were intact hybridized with the MoS_2 nanosheets, further validated using the DFT calculations in the upcoming section. Similarly, the O 1s XPS (Figure 5.16b_3) spectrum depicts three oxygen peaks; peaks at 531.77 eV and 533.47 eV correspond to the S-OH, S=O while the higher binding energies peak at 535.47eV corresponds to the -CF_2-O-CF_2 group appeared from Nafion, which was used as the binder for electrode fabrication.

5.3 Computational methodology

For obtaining further clarity and insight into our experimental findings, density functional theory (DFT) calculations were done using the plane-wave pseudopotential code, Vienna Ab Initio Simulation Package (VASP) [81, 82]. The interactions between core and valence electrons were described using the projected augmented wave method based on pseudopotentials [83]. The exchange-correlation interactions were treated by the generalized gradient approximation (GGA), within the Perdew−Burke−Ernzerhof (PBE) formalism [84]. Kinetic energy cut off of 520 eV is used to expand the plane waves included in the basis set. The supercell approach is used to model the MoS_2 surfaces such that the relaxed lattice parameter of the super-cell is a = 12.73 Å, b = 12.73 Å, and c = 34.69 Å respectively, such

that a vacuum layer of 20 Å is employed along the Z direction to create the surface slab. A Monkhorst pack k-grid of 3x3x1 was used for the Brillouin zone integration. After the relaxation of the pristine MoS_2 surface, the -SO_3H functional group is attached over it and further structural optimization is carried out. The optimized structure is shown in Figure 5.17. It can be seen that the functional group is stable and attached to the surface with an H atom pointing towards the surface.

Table 5.6: The Bader charges calculated for the MoS_2-SO_3H surface, for the atoms directly below the -SO_3H attachment

Bader charges		
Surface atoms		-SO_3H
S: -0.84, -0.84, -0.84	Mo: 1.74	S: 5.27 O: -1.94, -1.94, -1.89 H: 0.065

We did the computational analysis via DFT calculations to get further insight into the electronic structure and charge transfer properties. The Bader analysis is carried out and presented in Table 5.6. A positive Bader value means that the atom loses charge and a negative value indicates charge gain. It can be seen that the surface Mo atom loses, and S atoms gain charge, while in the -SO_3H group, there occurs a charge distribution between the S, O, and H atoms, making the functional group stable and attaches to the surface. The differential charge density analysis is also conducted to visualize the charge transfer at the surface and is shown in Figure 5.17. The yellow and blue regions represent the charge accumulation and depletion, respectively. It can be seen that the surface S atoms above which the H atoms are aligned accumulates charge as evidenced by the Bader analysis as well.

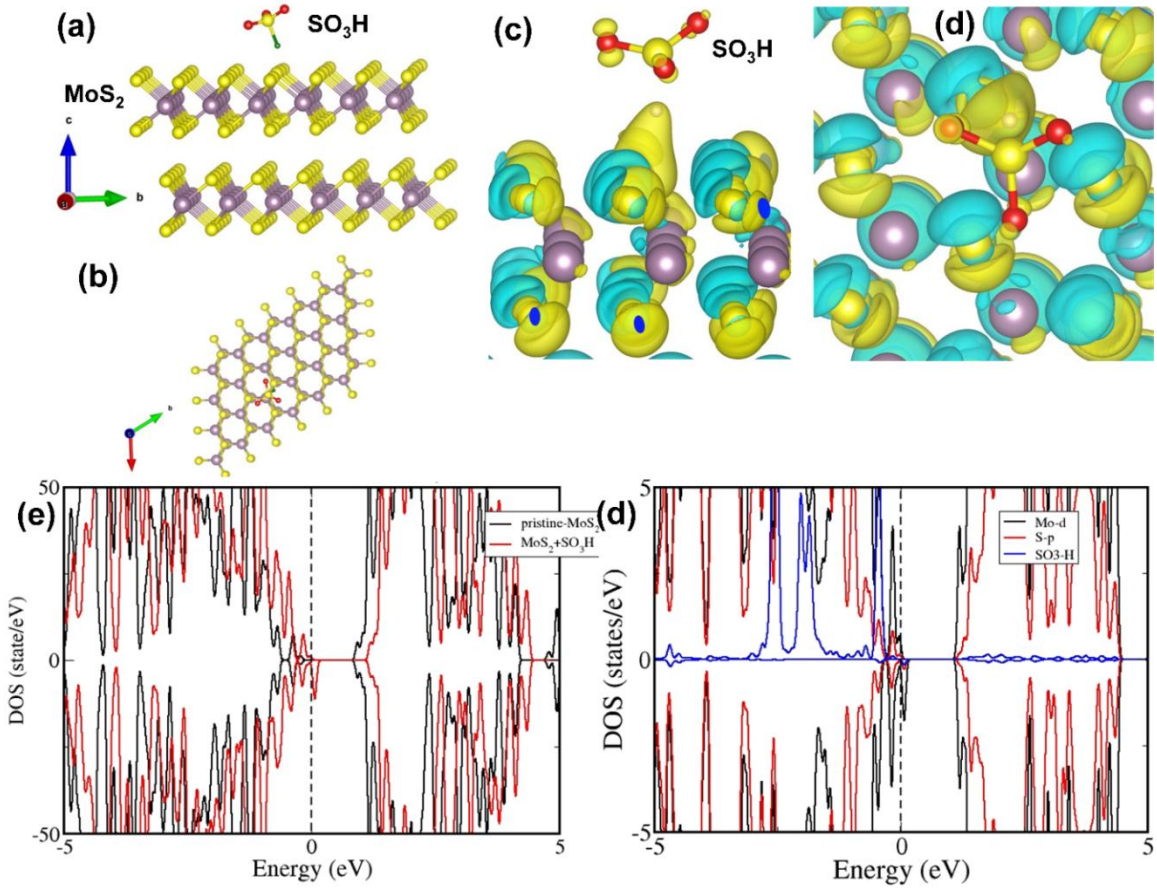

Figure 5.17: *(a) & (b) Show the respective side view and top view of the optimized structure of the MoS_2-SO_3H surface. (c) & (d) shows the side view and top view of the differential charge density plots calculated for the MoS_2-SO_3H surface. The isosurface level is 0.06 e/Å^3(e) total density of states of the pristine and SO_3H functionalized surface and (f) The orbital resolved partial density of states of the MoS_2+SO_3H surface.*

The DOS of the surfaces with and without -SO_3H is calculated to understand the changes in band structure brought about by the presence of the functional group. Figure 5.17 shows the total DOS for the pristine and functional group attached surfaces, and it is evident that VBM and CBM both are shifted with the attachment of functional group. The orbital and atom resolved DOS is shown in Figure 5.17. Significant hybridization occurs between the -SO_3H and *p* and *d* states of the S and Mo, and this pushes the valence band maximum towards higher energies, consequently narrowing the bandgap (Figure 5.18 a and Figure 5.18 b).

Furthermore, the Work function (WF) is calculated by subtracting the Fermi energy (E_F) from the vacuum potential (E_v) such that, WF = E_v – E_F. The vacuum potential is calculated for both pristine MoS_2 surface as well as for the -SO_3H functionalized surface and the plots are shown in the Figure 5.18 c and Figure 5.18 d. The E_V calculated for the MoS_2 surface is 3.88 eV and the E_F is -1.34 eV. Therefore, the WF is calculated as 5.21 eV. Similarly, the E_V calculated for the MoS_2+SO_3H surface is 2.86 eV and the E_F is -1.96 eV. Therefore, the calculated WF is 4.82 eV. Hence it can be seen that the functionalization with -SO_3H is reducing the WF of the surface and thereby enhancing its redox activity.

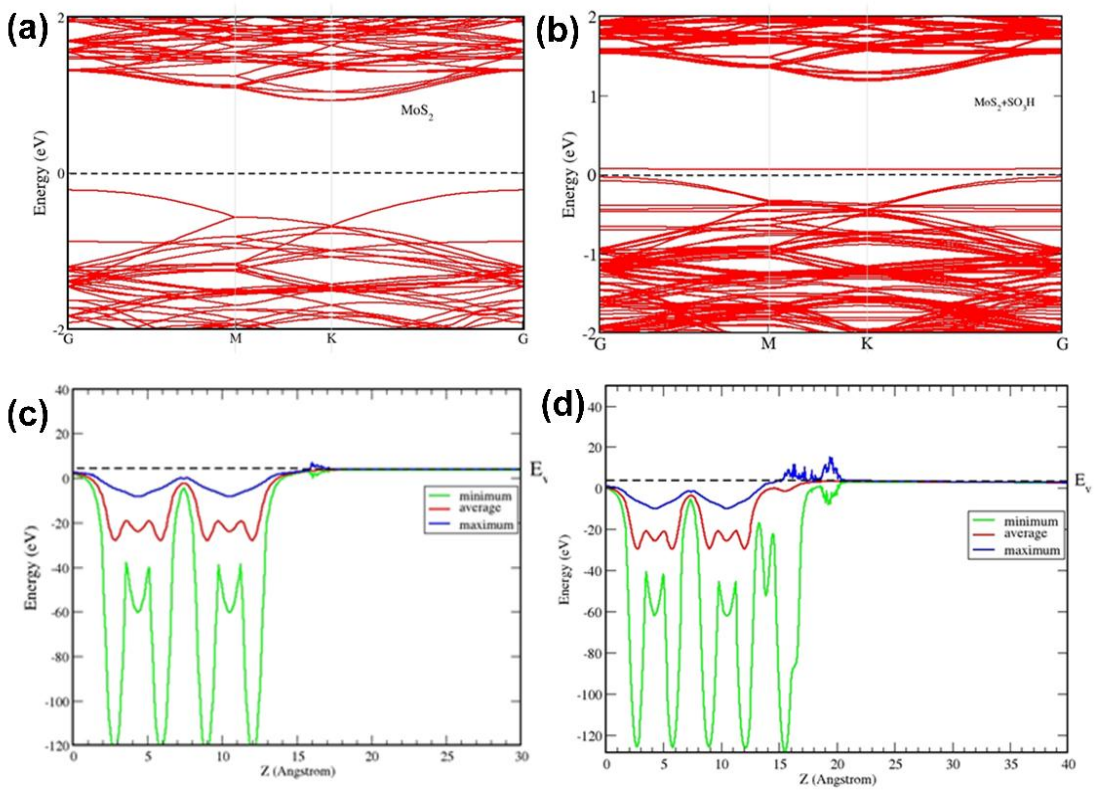

Figure 5.18: *(a) Band-structure of the MoS_2 surface; (b) Band-structure of the MoS_2+SO_3H surface; (c) Vacuum potential calculated for the MoS_2 surface; (d) Vacuum potential of the MoS_2+SO_3H surface.*

To sum it all, with increasing the thiourea molar ratio, the as-synthesized 2D-MoS_2 nanosheets get -SO_3H functionalized via chemical hybridizations and intercalation. We

obtained that the -SO_3H the functional group was attached to the MoS_2 nanosheet via *p* and *d* states of the S and Mo, respectively. The hybridization of -SO_3H functional group increases with increasing the thiourea molar ratio, and at 1:10 (i.e., for MoS_2-10 sample), the -SO_3H functional group hybridization gets saturated due to the transformation of -SO_3H functional group into SO_3^- functional group. In this regard, it is also obtained that the increase in the interlayer spacing in MoS_2 nanosheets also impregnate at 9.4 Å. The dual effects of hybridizations and intercalations successively modify the electronic structure of 2D-MoS_2 nanosheets and improve the electrocatalytic activities. Typically, -SO_3H hybridizations via *p* and *d* states shift the VBM and CBM, increasing the localized charge concentrations, further enhancing the catalytic charge transfer of such functionalized MoS_2 catalysts via Volmer-Heyrovsky mechanisms.

On the other hand, the successive intercalations of the -SO_3H functional group also broaden the interlayer spacing of MoS_2 nanosheets, which usually lowers the ΔG (energy barrier) of the catalyst's surface, thereby accelerating the H^+ absorptions/desorptions.[80] We believe that the simultaneous escalation of both the kinetics of charge transfer and lowering the surface energy barrier of H^+ adsorption /desorption and concurrently affect the improvement in the catalytic activities of the 2D-MoS_2 nanosheets with improved hydrogen evolution via electrocatalytic water splitting, as evident from the electrochemistry data. In addition, the increase in the interlayer spacing results in the improvement in the surface catalytic sites (Figure 5.13). It can also promote the enhancement in the electrocatalytic activity of functionalized MoS_2 catalyst compared to the pristine one. Furthermore, the catalysts electrode was stable under 12 h of the continuous test at specific current densities. After the stability test, it was found that the intact MoS_2 structure (physical, chemical, and physiochemical) with almost no change in hybridization properties or catalytic activities. Using DFT, we calculated WF for the pristine MoS_2 surface (~5.21 eV) as well as with -

SO_3H functionalized MoS_2 surface (~4.82 eV), where it was found that the reduction in WF occurred, indicating the enhanced redox-activity, which are well-supported with our experimental evidence as presented in this manuscript. We are confident that this work is novel, straightforward, and prompt, which will open a new chapter of functionalizations of 2D materials while consequently paving pathways towards new materials development via functionalizations of earth-abundant other 2D-TMDs for improved electrocatalytic activities for hydrogen production.

5.4 Chapter summary

In summary, we have developed in-situ -SO_3H functionalized MoS_2 catalysts with interlayer expanded features synthesized via a one-pot hydrothermal process with increasing thiourea content. Characterization techniques (such as Raman spectroscopy, FTIR, XPS, XRD, and TEM/HRTEM) endorsed the successful functionalization of MoS_2 nanosheets, where surface functionalizations and intercalations of -SO_3H functional group co-occurred with expanded interlayer distance via successive increase of thiourea. The 2D-MoS_2 nanosheets produced using molar ratio 1:8 of $(NH_4)_6Mo_7O_{24}.4H_2O$:CH_4N_2S showed the 4.84% of -SO_3H functional group contained in MoS_2 nanosheets, which demonstrated the high-performance electrocatalytic activity for HER. We also found that further increase in the thiourea ratio decreases the % of -SO_3H functional group and transforming -SO_3H functional group into SO_3^- functional group while deteriorating the electrocatalytic performance of the electrode too.

We believe that -SO_3H functionalized MoS_2 nanosheets with expanded interlayer distance enhances the surface area, interfacial charge transfer kinetics, and H^+ adsorption-desorption by lowering the ΔG (energy barrier), enhancing the surface conductivity, and improving the catalytically active sites. The overpotential, Tafel slope, and R_{ct} were obtained as ~82 mV (η_{10}), ~57 mV/dec, and 0.69 Ω, respectively, along with excellent stability of 12 h for the

SO_3H-MoS_2 (particularly for MoS_2-8), which are pretty close to equivalent Pt-wire. Using DFT, we calculated the work function for the pristine MoS_2 ~5.21 eV and -SO_3H functionalized MoS_2 ~4.82 eV. Such reduction in WF in SO_3H-MoS_2 indicates an increase in localized charge concentrations, which further improves the catalytic charge-transfer kinetics of such functionalized MoS_2 catalysts via Volmer-Heyrovsky mechanisms. We further believe that this work is unique, straightforward, and up-to-date, which will open a new paradigm of 2D-MoS_2 functionalizations, consequently paving pathways towards improving the catalytic activities of earth-abundant other 2D-TMDs for next-generation electrocatalysis.

References

[1] M. S. Faber and S. Jin, "Earth-abundant inorganic electrocatalysts and their nanostructures for energy conversion applications," *Energy & Environmental Science*, vol. 7, no. 11, pp. 3519-3542, 2014, doi: 10.1039/C4EE01760A.

[2] A. B. Laursen, S. Kegnæs, S. Dahl, and I. Chorkendorff, "Molybdenum sulfides-efficient and viable materials for electro - and photoelectrocatalytic hydrogen evolution," *Energy & Environmental Science*, vol. 5, no. 2, pp. 5577-5591, 2012, doi: 10.1039/C2EE02618J.

[3] D. Gopalakrishnan, D. Damien, and M. M. Shaijumon, "MoS_2 Quantum Dot-Interspersed Exfoliated MoS_2 Nanosheets," *ACS Nano*, vol. 8, no. 5, pp. 5297-5303, 2014, doi: 10.1021/nn501479e.

[4] L. Cheng *et al.*, "Ultrathin WS_2 Nanoflakes as a High-Performance Electrocatalyst for the Hydrogen Evolution Reaction," *Angewandte Chemie International Edition*, vol. 53, no. 30, pp. 7860-7863, 2014, doi: https://doi.org/10.1002/anie.201402315.

[5] D. Kong, J. J. Cha, H. Wang, H. R. Lee, and Y. Cui, "First-row transition metal dichalcogenide catalysts for hydrogen evolution reaction," *Energy & Environmental Science*, vol. 6, no. 12, pp. 3553-3558, 2013, doi: 10.1039/C3EE42413H.

[6] J. McAllister *et al.*, "Tuning and mechanistic insights of metal chalcogenide molecular catalysts for the hydrogen-evolution reaction," *Nature Communications*, vol. 10, no. 1, p. 370, 2019, doi: 10.1038/s41467-018-08208-4.

[7] J. Cao, J. Zhou, Y. Zhang, and X. Liu, "A facile one-step fabrication of a novel Cu/MoS_2 nano-assembled structure for enhanced hydrogen evolution reaction performance," *RSC Advances*, vol. 7, no. 42, pp. 25867-25871, 2017, doi: 10.1039/C7RA01605K.

[8] F. Z. Wang *et al.*, "Ammonia intercalated flower-like MoS_2 nanosheet film as electrocatalyst for high efficient and stable hydrogen evolution," *Scientific Reports*, vol. 6, no. 1, p. 31092, 2016, doi: 10.1038/srep31092.

[9] Y. Cao, "Roadmap and Direction toward High-Performance MoS_2 Hydrogen Evolution Catalysts," *ACS Nano*, vol. 15, no. 7, pp. 11014-11039, 2021, doi: 10.1021/acsnano.1c01879.

[10] H. Wang, C. Li, P. Fang, Z. Zhang, and J. Z. Zhang, "Synthesis, properties, and optoelectronic applications of two-dimensional MoS_2 and MoS_2-based heterostructures," *Chemical Society Reviews*, vol. 47, no. 16, pp. 6101-6127, 2018, doi: 10.1039/C8CS00314A.

[11] S. Das, M. Kim, J.-w. Lee, and W. Choi, "Synthesis, Properties, and Applications of 2D Materials: A Comprehensive Review," *Critical Reviews in Solid State and Materials Sciences*, vol. 39, no. 4, pp. 231-252, 2014, doi: 10.1080/10408436.2013.836075.

[12] X. Zhang and Y. Xie, "Recent advances in free-standing two-dimensional crystals with atomic thickness: design, assembly and transfer strategies," *Chemical Society Reviews*, vol. 42, no. 21, pp. 8187-8199, 2013, doi: 10.1039/C3CS60138B.

[13] C. Kumar, S. Das, and S. Jit, "7 - Device physics and device integration of two-dimensional heterostructures," in *2D Nanoscale Heterostructured Materials*, S. Jit and S. Das Eds.: Elsevier, 2020, pp. 195-214.

[14] J. Xie *et al.*, "Atomically-thin molybdenum nitride nanosheets with exposed active surface sites for efficient hydrogen evolution," *Chemical Science*, vol. 5, no. 12, pp. 4615-4620, 2014, doi: 10.1039/C4SC02019G.

[15] Q. H. Wang, K. Kalantar-Zadeh, A. Kis, J. N. Coleman, and M. S. Strano, "Electronics and optoelectronics of two-dimensional transition metal dichalcogenides," *Nature Nanotechnology,* vol. 7, no. 11, pp. 699-712, 2012, doi: 10.1038/nnano.2012.193.

[16] B. Hinnemann *et al.*, "Biomimetic Hydrogen Evolution: MoS_2 Nanoparticles as Catalyst for Hydrogen Evolution," *Journal of the American Chemical Society,* vol. 127, no. 15, pp. 5308-5309, 2005, doi: 10.1021/ja0504690.

[17] M.-R. Gao *et al.*, "An efficient molybdenum disulfide/cobalt diselenide hybrid catalyst for electrochemical hydrogen generation," *Nature Communications,* vol. 6, no. 1, p. 5982, 2015, doi: 10.1038/ncomms6982.

[18] J. Strachan, A. F. Masters, and T. Maschmeyer, "Critical review: hydrothermal synthesis of 1T-MoS_2 – an important route to a promising material," *Journal of Materials Chemistry A,* vol. 9, no. 15, pp. 9451-9461, 2021, doi: 10.1039/D1TA01230D.

[19] U. Sharma, S. Karazhanov, R. Jose, and S. Das, "Plasmonic hot-electron assisted phase transformation in 2D-MoS_2 for the hydrogen evolution reaction: current status and future prospects," *Journal of Materials Chemistry A,* vol. 10, no. 16, pp. 8626-8655, 2022, doi: 10.1039/D1TA10918A.

[20] J. D. Benck, Z. Chen, L. Y. Kuritzky, A. J. Forman, and T. F. Jaramillo, "Amorphous Molybdenum Sulfide Catalysts for Electrochemical Hydrogen Production: Insights into the Origin of their Catalytic Activity," *ACS Catalysis,* vol. 2, no. 9, pp. 1916-1923, 2012, doi: 10.1021/cs300451q.

[21] J. Xie *et al.*, "Defect-Rich MoS_2 Ultrathin Nanosheets with Additional Active Edge Sites for Enhanced Electrocatalytic Hydrogen Evolution," *Advanced Materials,* vol. 25, no. 40, pp. 5807-5813, 2013, doi: https://doi.org/10.1002/adma.201302685.

[22] D. Kong *et al.*, "Synthesis of MoS_2 and $MoSe_2$ Films with Vertically Aligned Layers," *Nano Letters,* vol. 13, no. 3, pp. 1341-1347, 2013, doi: 10.1021/nl400258t.

[23] P. Gnanasekar, D. Periyanagounder, and J. Kulandaivel, "Vertically aligned MoS_2 nanosheets on graphene for highly stable electrocatalytic hydrogen evolution reactions," *Nanoscale,* vol. 11, no. 5, pp. 2439-2446, 2019, doi: 10.1039/C8NR10092F.

[24] B. R. Garrett *et al.*, "Tunable Molecular MoS_2 Edge-Site Mimics for Catalytic Hydrogen Production," *Inorganic Chemistry*, vol. 55, no. 8, pp. 3960-3966, 2016, doi: 10.1021/acs.inorgchem.6b00206.

[25] F. Li *et al.*, "MoS_2 quantum dot decorated RGO: a designed electrocatalyst with high active site density for the hydrogen evolution reaction," *Journal of Materials Chemistry A*, vol. 3, no. 43, pp. 21772-21778, 2015, doi: 10.1039/C5TA05219J.

[26] J. Guo, F. Li, Y. Sun, X. Zhang, and L. Tang, "Oxygen-incorporated MoS_2 ultrathin nanosheets grown on graphene for efficient electrochemical hydrogen evolution," *Journal of Power Sources*, vol. 291, pp. 195-200, 2015, doi: https://doi.org/10.1016/j.jpowsour.2015.05.034.

[27] J. Cao, J. Zhou, Y. Zhang, and X. Liu, "A Clean and Facile Synthesis Strategy of MoS_2 Nanosheets Grown on Multi-Wall CNTs for Enhanced Hydrogen Evolution Reaction Performance," *Scientific Reports*, vol. 7, no. 1, p. 8825, 2017, doi: 10.1038/s41598-017-09047-x.

[28] A. Kagkoura, R. Arenal, and N. Tagmatarchis, "Controlled Chemical Functionalization toward 3D-2D Carbon Nanohorn-MoS_2 Heterostructures with Enhanced Electrocatalytic Activity for Protons Reduction," *Advanced Functional Materials*, vol. 31, no. 41, p. 2105287, 2021, doi: https://doi.org/10.1002/adfm.202105287.

[29] D. Hou *et al.*, "Pt nanoparticles/MoS_2 nanosheets/carbon fibers as efficient catalyst for the hydrogen evolution reaction," *Electrochimica Acta*, vol. 166, pp. 26-31, 2015, doi: https://doi.org/10.1016/j.electacta.2015.03.067.

[30] N. Zhang, S. Gan, T. Wu, W. Ma, D. Han, and L. Niu, "Growth Control of MoS_2 Nanosheets on Carbon Cloth for Maximum Active Edges Exposed: An Excellent Hydrogen Evolution 3D Cathode," *ACS Applied Materials & Interfaces*, vol. 7, no. 22, pp. 12193-12202, 2015, doi: 10.1021/acsami.5b02586.

[31] W. Li, Z. Zhang, W. Zhang, and S. Zou, "MoS_2 Nanosheets Supported on Hollow Carbon Spheres as Efficient Catalysts for Electrochemical Hydrogen Evolution Reaction," *ACS Omega*, vol. 2, no. 8, pp. 5087-5094, 2017, doi: 10.1021/acsomega.7b00755.

[32] J.-Y. Xue *et al.*, "In Situ Generation of Bifunctional Fe-Doped MoS_2 Nanocanopies for Efficient Electrocatalytic Water Splitting," *Inorganic Chemistry*, vol. 58, no. 16, pp. 11202-11209, 2019, doi: 10.1021/acs.inorgchem.9b01814.

[33] H. Wang *et al.*, "Transition-metal doped edge sites in vertically aligned MoS_2 catalysts for enhanced hydrogen evolution," *Nano Research*, vol. 8, no. 2, pp. 566-575, 2015, doi: 10.1007/s12274-014-0677-7.

[34] Q. Yang *et al.*, "Activating MoS_2 with Super-High Nitrogen-Doping Concentration as Efficient Catalyst for Hydrogen Evolution Reaction," *The Journal of Physical Chemistry C*, vol. 123, no. 17, pp. 10917-10925, 2019, doi: 10.1021/acs.jpcc.9b00059.

[35] K. Guruprasad, T. Maiyalagan, and S. Shanmugam, "Phosphorus Doped MoS_2 Nanosheet Promoted with Nitrogen, Sulfur Dual Doped Reduced Graphene Oxide as an Effective Electrocatalyst for Hydrogen Evolution Reaction," *ACS Applied Energy Materials*, vol. 2, no. 9, pp. 6184-6194, 2019, doi: 10.1021/acsaem.9b00629.

[36] J. Xu, J. Zhang, W. Zhang, and C.-S. Lee, "Interlayer Nanoarchitectonics of Two-Dimensional Transition-Metal Dichalcogenides Nanosheets for Energy Storage and Conversion Applications," *Advanced Energy Materials*, vol. 7, no. 23, p. 1700571, 2017, doi: https://doi.org/10.1002/aenm.201700571.

[37] D. Sarkar *et al.*, "Expanding Interlayer Spacing in MoS_2 for Realizing an Advanced Supercapacitor," *ACS Energy Letters*, vol. 4, no. 7, pp. 1602-1609, 2019, doi: 10.1021/acsenergylett.9b00983.

[38] Y.-J. Tang *et al.*, "Molybdenum Disulfide/Nitrogen-Doped Reduced Graphene Oxide Nanocomposite with Enlarged Interlayer Spacing for Electrocatalytic Hydrogen Evolution," *Advanced Energy Materials*, vol. 6, no. 12, p. 1600116, 2016, doi: https://doi.org/10.1002/aenm.201600116.

[39] U. Gupta, D. Gautam, V. Jain, and B. Mukherjee, "2 - Design and synthesis of two-dimensional materials and their heterostructures," in *2D Nanoscale Heterostructured Materials*, S. Jit and S. Das Eds.: Elsevier, 2020, pp. 13-54.

[40] J. Liu, Z. Wang, J. Li, L. Cao, Z. Lu, and D. Zhu, "Structure Engineering of MoS_2 via Simultaneous Oxygen and Phosphorus Incorporation for Improved Hydrogen Evolution," *Small,* vol. 16, no. 4, p. 1905738, 2020, doi: https://doi.org/10.1002/smll.201905738.

[41] K. D. Rasamani, F. Alimohammadi, and Y. Sun, "Interlayer-expanded MoS_2," *Materials Today,* vol. 20, no. 2, pp. 83-91, 2017, doi: https://doi.org/10.1016/j.mattod.2016.10.004.

[42] C. Tsai, F. Abild-Pedersen, and J. K. Nørskov, "Tuning the MoS_2 Edge-Site Activity for Hydrogen Evolution via Support Interactions," *Nano Letters,* vol. 14, no. 3, pp. 1381-1387, 2014, doi: 10.1021/nl404444k.

[43] J. Xie *et al.*, "Controllable Disorder Engineering in Oxygen-Incorporated MoS_2 Ultrathin Nanosheets for Efficient Hydrogen Evolution," *Journal of the American Chemical Society,* vol. 135, no. 47, pp. 17881-17888, 2013, doi: 10.1021/ja408329q.

[44] M.-R. Gao, M. K. Y. Chan, and Y. Sun, "Edge-terminated molybdenum disulfide with a 9.4-Å interlayer spacing for electrochemical hydrogen production," *Nature Communications,* vol. 6, no. 1, p. 7493, 2015, doi: 10.1038/ncomms8493.

[45] N. H. Attanayake *et al.*, "Effect of Intercalated Metals on the Electrocatalytic Activity of 1T-MoS_2 for the Hydrogen Evolution Reaction," *ACS Energy Letters,* vol. 3, no. 1, pp. 7-13, 2018, doi: 10.1021/acsenergylett.7b00865.

[46] P. Vishnoi, A. Sampath, U. V. Waghmare, and C. N. R. Rao, "Covalent Functionalization of Nanosheets of MoS_2 and $MoSe_2$ by Substituted Benzenes and Other Organic Molecules," *Chemistry – A European Journal,* vol. 23, no. 4, pp. 886-895, 2017, doi: https://doi.org/10.1002/chem.201604176.

[47] Y. L. Huang, Y. J. Zheng, Z. Song, D. Chi, A. T. S. Wee, and S. Y. Quek, "The organic–2D transition metal dichalcogenide heterointerface," *Chemical Society Reviews,* vol. 47, no. 9, pp. 3241-3264, 2018, doi: 10.1039/C8CS00159F.

[48] B. Vedhanarayanan, J. Shi, J.-Y. Lin, S. Yun, and T.-W. Lin, "Enhanced activity and stability of MoS_2 through enriching 1T-phase by covalent functionalization for energy conversion applications," *Chemical Engineering Journal,* vol. 403, p. 126318, 2021, doi: https://doi.org/10.1016/j.cej.2020.126318.

[49] E. E. Benson *et al.*, "Balancing the Hydrogen Evolution Reaction, Surface Energetics, and Stability of Metallic MoS_2 Nanosheets via Covalent Functionalization," *Journal of the American Chemical Society*, vol. 140, no. 1, pp. 441-450, 2018, doi: 10.1021/jacs.7b11242.

[50] Z. Sun, M. Yang, Y. Wang, and Y. H. Hu, "Novel Binder-Free Three-Dimensional MoS_2-Based Electrode for Efficient and Stable Electrocatalytic Hydrogen Evolution," *ACS Applied Energy Materials*, vol. 2, no. 2, pp. 1102-1110, 2019, doi: 10.1021/acsaem.8b01670.

[51] A. Ghorai, S. K. Ray, and A. Midya, "Ethylenediamine-Assisted High Yield Exfoliation of MoS_2 for Flexible Solid-State Supercapacitor Application," *ACS Applied Nano Materials*, vol. 2, no. 3, pp. 1170-1177, 2019, doi: 10.1021/acsanm.8b02002.

[52] L. Zhang *et al.*, "2D atomic crystal molecular superlattices by soft plasma intercalation," *Nature Communications*, vol. 11, no. 1, p. 5960, 2020, doi: 10.1038/s41467-020-19766-x.

[53] A. Gopalakrishnan, L. Durai, J. Ma, C. Y. Kong, and S. Badhulika, "Vertically Aligned Few-Layer Crumpled MoS_2 Hybrid Nanostructure on Porous Ni Foam toward Promising Binder-Free Methanol Electro-Oxidation Application," *Energy & Fuels*, vol. 35, no. 12, pp. 10169-10180, 2021, doi: 10.1021/acs.energyfuels.1c00957.

[54] D. L. Eldridge, B. O. Mysen, and G. D. Cody, "Experimental estimation of the bisulfite isomer quotient as a function of temperature: Implications for sulfur isotope fractionations in aqueous sulfite solutions," *Geochimica et Cosmochimica Acta*, vol. 220, pp. 309-328, 2018, doi: https://doi.org/10.1016/j.gca.2017.10.005.

[55] W. Feng *et al.*, "Flower-like PEGylated MoS_2 nanoflakes for near-infrared photothermal cancer therapy," *Scientific Reports*, vol. 5, no. 1, p. 17422, 2015, doi: 10.1038/srep17422.

[56] M. Zhao *et al.*, "Solvothermal synthesis of oxygen-incorporated MoS_{2-x} nanosheets with abundant undercoordinated Mo for efficient hydrogen evolution," *International Journal of Hydrogen Energy*, vol. 45, no. 38, pp. 19133-19143, 2020, doi: https://doi.org/10.1016/j.ijhydene.2020.05.003.

[57] K.-J. Huang, L. Wang, Y.-J. Liu, H.-B. Wang, Y.-M. Liu, and L.-L. Wang, "Synthesis of polyaniline/2-dimensional graphene analog MoS_2 composites for high-performance

supercapacitor," *Electrochimica Acta*, vol. 109, pp. 587-594, 2013, doi: https://doi.org/10.1016/j.electacta.2013.07.168.

[58] D. K. Patel *et al.*, "Functionalized Graphene Tagged Polyurethanes for Corrosion Inhibitor and Sustained Drug Delivery," *ACS Biomaterials Science & Engineering*, vol. 3, no. 12, pp. 3351-3363, 2017, doi: 10.1021/acsbiomaterials.7b00342.

[59] Q. Guan *et al.*, "Sulfonated multi-walled carbon nanotubes for biodiesel production through triglycerides transesterification," *RSC Advances*, vol. 7, no. 12, pp. 7250-7258, 2017, doi: 10.1039/C6RA28067F.

[60] S. Daripa, V. K. Singh, O. Prakash, P. Maiti, B. K. Kuila, and S. Das, "Sulfonated graphene-modified electrodes for enhanced capacitive performance and improved electro-oxidation of hydrogen peroxide," *Nano-Structures & Nano-Objects*, vol. 24, p. 100531, 2020, doi: https://doi.org/10.1016/j.nanoso.2020.100531.

[61] M. Liu, S. Jia, Y. Gong, C. Song, and X. Guo, "Effective Hydrolysis of Cellulose into Glucose over Sulfonated Sugar-Derived Carbon in an Ionic Liquid," *Industrial & Engineering Chemistry Research*, vol. 52, no. 24, pp. 8167-8173, 2013, doi: 10.1021/ie400571e.

[62] S. Imaizumi, H. Matsumoto, M. Ashizawa, M. Minagawa, and A. Tanioka, "Nanosize effects of sulfonated carbon nanofiber fabrics for high capacity ion-exchanger," *RSC Advances*, vol. 2, no. 7, pp. 3109-3114, 2012, doi: 10.1039/C2RA20103H.

[63] H. G. Kang *et al.*, "Feasibility tests of $–SO_3H/–SO_3–$-functionalized magnesium phyllosilicate [$–SO_3H/–SO_3–$ MP] for environmental and bioenergy applications," *RSC Advances*, vol. 5, no. 78, pp. 63271-63277, 2015, doi: 10.1039/C5RA07390A.

[64] Y. Qi, Q. Xu, Y. Wang, B. Yan, Y. Ren, and Z. Chen, "CO_2-Induced Phase Engineering: Protocol for Enhanced Photoelectrocatalytic Performance of 2D MoS_2 Nanosheets," *ACS Nano*, vol. 10, no. 2, pp. 2903-2909, 2016, doi: 10.1021/acsnano.6b00001.

[65] V. K. Singh, U. Gupta, B. Mukherjee, S. Chattopadhyay, and S. Das, "MoS_2 Nanosheets on $MoNi_4/MoO_2$ Nanorods for Hydrogen Evolution," *ACS Applied Nano Materials*, vol. 4, no. 1, pp. 886-896, 2021, doi: 10.1021/acsanm.0c03296.

[66] D. Zhang *et al.*, "High performance catalytic distillation using CNTs-based holistic catalyst for production of high quality biodiesel," *Scientific Reports*, vol. 4, no. 1, p. 4021, 2014, doi: 10.1038/srep04021.

[67] H. Yu, Y. Jin, Z. Li, F. Peng, and H. Wang, "Synthesis and characterization of sulfonated single-walled carbon nanotubes and their performance as solid acid catalyst," *Journal of Solid State Chemistry*, vol. 181, no. 3, pp. 432-438, 2008, doi: https://doi.org/10.1016/j.jssc.2007.12.017.

[68] X. Zhang *et al.*, "Hydrothermal synthesis and characterization of 3D flower-like MoS_2 microspheres," *Materials Letters*, vol. 148, pp. 67-70, 2015, doi: https://doi.org/10.1016/j.matlet.2015.02.027.

[69] S. Duraisamy, A. Ganguly, P. K. Sharma, J. Benson, J. Davis, and P. Papakonstantinou, "One-Step Hydrothermal Synthesis of Phase-Engineered MoS_2/MoO_3 Electrocatalysts for Hydrogen Evolution Reaction," *ACS Applied Nano Materials*, vol. 4, no. 3, pp. 2642-2656, 2021, doi: 10.1021/acsanm.0c03274.

[70] P. Sun, W. Zhang, X. Hu, L. Yuan, and Y. Huang, "Synthesis of hierarchical MoS_2 and its electrochemical performance as an anode material for lithium-ion batteries," *Journal of Materials Chemistry A*, vol. 2, no. 10, pp. 3498-3504, 2014, doi: 10.1039/C3TA13994H.

[71] H. A. Therese, N. Zink, U. Kolb, and W. Tremel, "Synthesis of MoO_3 nanostructures and their facile conversion to MoS_2 fullerenes and nanotubes," *Solid State Sciences*, vol. 8, no. 10, pp. 1133-1137, 2006, doi: https://doi.org/10.1016/j.solidstatesciences.2006.05.011.

[72] Z. Chen, D. Cummins, B. N. Reinecke, E. Clark, M. K. Sunkara, and T. F. Jaramillo, "Core–shell MoO_3–MoS_2 Nanowires for Hydrogen Evolution: A Functional Design for Electrocatalytic Materials," *Nano Letters*, vol. 11, no. 10, pp. 4168-4175, 2011, doi: 10.1021/nl2020476.

[73] W. Fu *et al.*, "Surface-Electron Coupling for Efficient Hydrogen Evolution," *Angewandte Chemie International Edition*, vol. 58, no. 49, pp. 17709-17717, 2019, doi: https://doi.org/10.1002/anie.201908938.

[74] S. Yun, Y. Zhang, L. Zhang, Z. Liu, and Y. Deng, "Ni and Fe nanoparticles, alloy and Ni/Fe-N_x coordination co-boost the catalytic activity of the carbon-based catalyst for triiodide reduction and hydrogen evolution reaction," *Journal of Colloid and Interface Science,* vol. 615, pp. 501-516, 2022, doi: https://doi.org/10.1016/j.jcis.2022.01.192.

[75] Y. Zhang *et al.*, "Implanted metal-nitrogen active sites enhance the electrocatalytic activity of zeolitic imidazolate zinc framework-derived porous carbon for the hydrogen evolution reaction in acidic and alkaline media," *Journal of Colloid and Interface Science,* vol. 604, pp. 441-457, , doi: https://doi.org/10.1016/j.jcis.2021.06.152.

[76] S. Yun *et al.*, "Insight into electrocatalytic activity and mechanism of bimetal niobium-based oxides in situ embedded into biomass-derived porous carbon skeleton nanohybrids for photovoltaics and alkaline hydrogen evolution," *Journal of Colloid and Interface Science,* vol. 601, pp. 12-29, 2021, doi: https://doi.org/10.1016/j.jcis.2021.05.060.

[77] J. L. C. Fajín, M. N. D. S. Cordeiro, and J. R. B. Gomes, "Density Functional Theory Study of the Water Dissociation on Platinum Surfaces: General Trends," *The Journal of Physical Chemistry A,* vol. 118, no. 31, pp. 5832-5840, 2014, doi: 10.1021/jp411500j.

[78] Y.-Y. Chen *et al.*, "Self-Templated Fabrication of $MoNi_4/MoO_{3-x}$ Nanorod Arrays with Dual Active Components for Highly Efficient Hydrogen Evolution," *Advanced Materials,* vol. 29, no. 39, p. 1703311, 2017, doi: https://doi.org/10.1002/adma.201703311.

[79] X. Wang *et al.*, "Boosting catalytic activity of niobium/tantalum-nitrogen active-sites for triiodide reduction in photovoltaics," *Journal of Colloid and Interface Science,* vol. 603, pp. 651-665, 2021, doi: https://doi.org/10.1016/j.jcis.2021.06.128.

[80] F. Han *et al.*, "Efficient dual-function catalysts for triiodide reduction reaction and hydrogen evolution reaction using unique 3D network aloe waste-derived carbon-supported molybdenum-based bimetallic oxide nanohybrids," *Applied Catalysis B: Environmental,* vol. 273, p. 119004, 2020, doi: https://doi.org/10.1016/j.apcatb.2020.119004.

[81] G. Kresse, "Ab initio molecular dynamics for liquid metals," *Journal of Non-Crystalline Solids,* vol. 192-193, pp. 222-229, 1995, doi: https://doi.org/10.1016/0022-3093(95)00355-X.

[82] G. Kresse and J. Furthmüller, "Efficiency of ab-initio total energy calculations for metals and semiconductors using a plane-wave basis set," *Computational Materials Science*, vol. 6, no. 1, pp. 15-50, 1996, doi: https://doi.org/10.1016/0927-0256(96)00008-0.

[83] G. Kresse and D. Joubert, "From ultrasoft pseudopotentials to the projector augmented-wave method," *Physical Review B*, vol. 59, no. 3, pp. 1758-1775,1999, doi: 10.1103/PhysRevB.59.1758.

[84] J. P. Perdew, K. Burke, and M. Ernzerhof, "Generalized Gradient Approximation Made Simple," *Physical Review Letters*, vol. 77, no. 18, pp. 3865-3868, 1996, doi: 10.1103/PhysRevLett.77.3865.